

KELT-6b: A P~7.9 d HOT SATURN TRANSITING A METAL-POOR STAR WITH A LONG-PERIOD COMPANION*

KAREN A. COLLINS¹, JASON D. EASTMAN^{2,3}, THOMAS G. BEATTY⁴, ROBERT J. SIVERD⁵, B. SCOTT GAUDI⁴, JOSHUA PEPPER^{5,6}, JOHN F. KIELKOPF¹, JOHN ASHER JOHNSON^{7,8}, ANDREW W. HOWARD⁹, DEBRA A. FISCHER¹⁰, MARK MANNER^{11,12}, ALLYSON BIERYLA¹³, DAVID W. LATHAM¹³, BENJAMIN J. FULTON⁹, JOAO GREGORIO¹⁴, LARS A. BUCHHAVE^{15,16}, ERIC L. N. JENSEN¹⁷, KEIVAN G. STASSUN^{5,18}, KALOYAN PENEV¹⁹, JUSTIN R. CREPP²⁰, SASHA HINKLEY^{7,21}, RACHEL A. STREET², PHILLIP CARGILE⁵, CLAUDE E. MACK⁵, THOMAS E. OBERST²², RYAN L. AVRIL²², SAMUEL N. MELLON²², KIM K. MCLEOD²³, MATTHEW T. PENNY⁴, ROBERT P. STEFANIK¹³, PERRY BERLIND¹³, MICHAEL L. CALKINS¹³, QINGQING MAO⁵, ALEXANDER J. W. RICHERT²⁴, DARREN L. DEPOY²⁵, GILBERT A. ESQUERDO⁴, ANDREW GOULD⁴, JENNIFER L. MARSHALL²⁵, RYAN J. OELKERS²⁵, RICHARD W. POGGE⁴, MARK TRUEBLOOD²⁶, AND PATRICIA TRUEBLOOD²⁶

Draft version May 18, 2018

ABSTRACT

We report the discovery of KELT-6b, a mildly-inflated Saturn-mass planet transiting a metal-poor host. The initial transit signal was identified in KELT-North survey data, and the planetary nature of the occulter was established using a combination of follow-up photometry, high-resolution imaging, high-resolution spectroscopy, and precise radial velocity measurements. The fiducial model from a global analysis including constraints from isochrones indicates that the $V = 10.38$ host star (BD+31 2447) is a mildly evolved, late-F star with $T_{\text{eff}} = 6102 \pm 43$ K, $\log g_{\star} = 4.07^{+0.04}_{-0.07}$ and $[\text{Fe}/\text{H}] = -0.28 \pm 0.04$, with an inferred mass $M_{\star} = 1.09 \pm 0.04 M_{\odot}$ and radius $R_{\star} = 1.58^{+0.16}_{-0.09} R_{\odot}$. The planetary companion has mass $M_{\text{p}} = 0.43 \pm 0.05 M_{\text{Jup}}$, radius $R_{\text{p}} = 1.19^{+0.13}_{-0.08} R_{\text{Jup}}$, surface gravity $\log g_{\text{p}} = 2.86^{+0.06}_{-0.08}$, and density $\rho_{\text{p}} = 0.31^{+0.07}_{-0.08} \text{ g cm}^{-3}$. The planet is on an orbit with semimajor axis $a = 0.079 \pm 0.001 \text{ AU}$ and eccentricity $e = 0.22^{+0.12}_{-0.10}$, which is roughly consistent with circular, and has ephemeris of $T_{\text{c}}(\text{BJD}_{\text{TDB}}) = 2456347.79679 \pm 0.00036$ and $P = 7.845631 \pm 0.000046$ d. Equally plausible fits that employ empirical constraints on the host star parameters rather than isochrones yield a larger planet mass and radius by $\sim 4-7\%$. KELT-6b has surface gravity and incident flux similar to HD 209458b, but orbits a host that is more metal poor than HD 209458 by ~ 0.3 dex. Thus, the KELT-6 system offers an opportunity to perform a comparative measurement of two similar planets in similar environments around stars of very different metallicities. The precise radial velocity data also reveal an acceleration indicative of a longer-period third body in the system, although the companion is not detected in Keck adaptive optics images.

Subject headings: instrumentation: adaptive optics, planetary systems, stars: individual (KELT-6, BD+31 2447, TYC 2532-556-1, HD 209458), techniques: photometric, techniques: spectroscopic

1. INTRODUCTION

Ground-based surveys have discovered dozens of transiting exoplanets around bright ($V < 11$) stars. Those discoveries are of considerable importance because they enable cost-effective detailed measurements of physical properties of extrasolar planets and their host stars (see reviews by Winn 2009, 2010). Discoveries of transiting exoplanets that have characteristics similar to an already well-measured exoplanet, but that differ significantly in one aspect, are of particularly high importance because they enable comparative studies.

The high scientific value of transiting planet systems motivated the first dedicated wide-field transit surveys, which have now produced a large number of discoveries (TrES, Alonso et al. 2004; XO, McCullough et al. 2006; HATNet, Bakos et al. 2007; SuperWASP, Collier Cameron et al. 2007a, QES, Al-

*KELT is a joint project of The Ohio State University, Vanderbilt University, and Lehigh University.

¹ Department of Physics & Astronomy, University of Louisville, Louisville, KY 40292, USA

² Las Cumbres Observatory Global Telescope Network, 6740 Cortona Drive, Suite 102, Santa Barbara, CA 93117, USA

³ Department of Physics Broida Hall, University of California, Santa Barbara, CA 93106, USA

⁴ Department of Astronomy, The Ohio State University, 140 W. 18th Ave., Columbus, OH 43210, USA

⁵ Department of Physics and Astronomy, Vanderbilt University, Nashville, TN 37235, USA

⁶ Department of Physics, Lehigh University, Bethlehem, PA, 18015, USA

⁷ Department of Astrophysics, California Institute of Technology, Pasadena, CA 91125, USA

⁸ NASA Exoplanet Science Institute (NExScI), CIT Mail Code 100-22, 770 South Wilson Avenue, Pasadena, CA 91125, USA

⁹ Institute for Astronomy, University of Hawaii, 2680 Woodlawn Drive, Honolulu, HI 96822, USA

¹⁰ Department of Astronomy, Yale University, New Haven, Connecticut 06511, USA

¹¹ Spot Observatory, Nunnally, TN, USA

¹² Montgomery Bell Academy, Nashville, TN, USA

¹³ Harvard-Smithsonian Center for Astrophysics, 60 Garden Street, Cambridge, MA 02138, USA

¹⁴ Atalaia Group & Crow-Observatory, Portalegre, Portugal

¹⁵ Niels Bohr Institute, University of Copenhagen, Juliane Maries vej 30, 21500 Copenhagen, Denmark

¹⁶ Centre for Star and Planet Formation, Geological Museum, Øster Voldgade 5, 1350 Copenhagen, Denmark

¹⁷ Department of Physics and Astronomy, Swarthmore College, Swarthmore, PA 19081, USA

¹⁸ Department of Physics, Fisk University, Nashville, TN 37208, USA

¹⁹ Princeton University, Princeton, NJ, USA

²⁰ Department of Physics, University of Notre Dame, 225 Nieuwland Science Hall, Notre Dame, IN 46556, USA

²¹ NSF Fellow

²² Westminster College, New Wilmington, PA, USA

²³ Wellesley College, Wellesley, MA, USA

²⁴ Department of Astronomy and Astrophysics, Pennsylvania State University, University Park, PA, USA

²⁵ George P. and Cynthia Woods Mitchell Institute for Fundamental Physics and Astronomy, and Department of Physics & Astronomy, Texas A & M University, College Station, TX 77843-4242, USA

²⁶ Winer Observatory, Sonoita, AZ 85637, USA

subai et al. 2011). SuperWASP and HATNet have been especially productive, with each survey discovering dozens of new transiting planets. The space-based missions CoRoT (Baglin 2003) and Kepler (Borucki et al. 2010) have dramatically expanded the parameter space of transit surveys, enabling the detection of transiting planets with sizes down to that of the Earth and below, planets with periods of several years, and planets orbiting host stars with a wider range of physical characteristics.

The Kilodegree Extremely Little Telescope-North (KELT-North) transit survey (Pepper et al. 2007) is designed to detect transiting planets around bright stars. Pepper et al. (2003) designed the aperture, optical system, and exposure time for KELT-North to provide better than 1% RMS photometry for stars with $8 < V < 10$. That magnitude range represents the brightness gap between comprehensive RV surveys and most other transit surveys. The KELT-North telescope system was constructed using commercial off-the-shelf equipment and has been collecting data since September 2006.

The KELT-North survey has already announced three low-mass transiting companions. KELT-1b (Sivard et al. 2012) is a highly inflated $27 M_J$ brown dwarf transiting a $V = 10.7$ mid-F star. KELT-2Ab (Beatty et al. 2012) is a hot Jupiter transiting the bright ($V = 8.77$) primary star of a binary system. KELT-3b (Pepper et al. 2013) is a hot Jupiter planet transiting a $V = 9.8$ late-F star. The designations KELT-4 and KELT-5 are currently reserved for two candidates in the confirmation phase.

Because KELT-North has focused on the same fields for an extended length of time (> 6 years), longer period ($P \geq 5$ d) planets are now detectable in the data. The large number of observations of each field also enables the detection of smaller planet-to-star radius ratios. In this paper we describe the discovery and characterization of KELT-6b, a transiting mildly-inflated Saturn-mass planet orbiting a $V = 10.38$ metal-poor host BD+31 2447 (hereafter KELT-6). KELT-6b is currently the sixth longest period exoplanet discovered by a ground-based transit survey, after HAT-P-15b, HAT-P-17b, WASP-8b, WASP-59b, and WASP-84b²⁷. In several important aspects, KELT-6b resembles a metal-poor analog of one of the most well-studied transiting planets, HD 209458b (Charbonneau et al. 2000; Henry et al. 2000). Both hosts have similar effective temperatures of ~ 6100 K, although KELT-6 is significantly more evolved and therefore has a larger radius. On the other hand, KELT-6b has a substantially larger orbit than HD 209458b. As a result, the incident fluxes at both planets are very similar. In addition, the surface gravity of KELT-6b differs from that of HD 209458b by only $\sim 20\%$.

The discovery of KELT-6b offers an opportunity to perform a comparative measurement of two similar planets in similar environments around stars of very different metallicities. The comparison may, for example, elucidate the effect of bulk composition of the planet atmosphere on the cause of atmospheric temperature inversions (e.g., Madhusudhan & Seager 2010). In addition, host-star metallicity has been shown to affect the physical and orbital properties of planets. In particular, there is a rough correlation between metallicity and estimated core mass (Burrows et al. 2007; Torres et al. 2008; Sato et al. 2005), and there are indications of trends in the

properties of planets with metallicity, which may signal the existence of multiple mechanisms for the formation and/or delivery of close-in giant planets (e.g., Ribas & Miralda-Escudé 2007; Dawson & Murray-Clay 2013).

2. DISCOVERY AND FOLLOW-UP OBSERVATIONS

We provide a brief summary of the KELT survey data reduction process in §2.1; for more details, see §2 of Sivard et al. (2012).

2.1. KELT-North Observations and Photometry

KELT-6 is in KELT-North survey field 08, which is centered on ($\alpha = 13^h38^m28^s.25$, $\delta = +31^\circ41'12''.67$; J2000). We monitored field 08 from December 2006, to June 2011, collecting a total of 7359 observations. We reduced the raw survey data using a custom implementation of the ISIS image subtraction package (Alard & Lupton 1998; Alard 2000), combined with point-spread fitting photometry using DAOPHOT (Stetson 1987). Using proper motions from the Tycho-2 catalog (Høg et al. 2000) and J and H magnitudes from 2MASS (Skrutskie et al. 2006; Cutri et al. 2003), we implemented a reduced proper motion cut (Gould & Morgan 2003) based on the specific implementation of Collier Cameron et al. (2007b), in order to select likely dwarf and subgiant stars within the field for further post-processing and analysis. We applied the trend filtering algorithm (TFA; Kovács et al. 2005) to each remaining light curve to remove systematic noise, followed by a search for transit signals using the box-fitting least squares algorithm (BLS; Kovács et al. 2002). For both TFA and BLS we used the versions found in the VARTOOLS package (Hartman et al. 2008).

One of the candidates from field 08 was star BD+31 2447 / TYC 2532-556-1, located at ($\alpha = 13^h03^m55^s.65$, $\delta = +30^\circ38'24''.3$; J2000). The star has Tycho magnitudes $B_T = 10.736 \pm 0.048$ and $V_T = 10.294 \pm 0.050$ (Høg et al. 2000), and passed our initial selection cuts. The discovery light curve of KELT-6 is shown in Figure 1. We observed a transit-like feature at a period of 7.8457 days, with a depth of about 5 mmag.

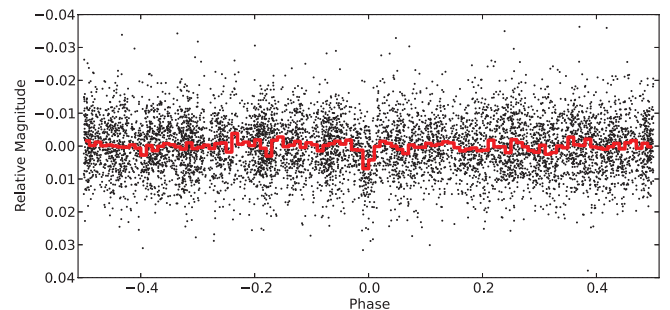


Figure 1. Discovery light curve of KELT-6 from the KELT-North telescope. The light curve contains 7359 observations spanning 4.5 years, phase-folded to the orbital period of 7.8457 days. The solid red line represents the same data binned at ~ 2 -hour intervals after phase-folding.

2.2. Radial-Velocity Observations

After KELT-6 was selected as a candidate, we conducted radial-velocity (RV) observations to identify possible false-positive signatures and to determine the RV orbit. We obtained data using the Tillinghast Reflector Echelle Spectro-

²⁷ The Exoplanet Orbit Database (Wright et al. 2011; <http://exoplanets.org/>) lists four planets with longer periods as of November 5th, 2013. WASP-84b (Anderson et al. 2013) is not in the database at the time of writing, but we include it here for completeness.

graph²⁸ (TRES; Fűrész 2008), on the 1.5m Tillinghast Reflector at the Fred L. Whipple Observatory (FLWO) at Mt. Hopkins, AZ. We observed KELT-6 three times with TRES over three months, from UT 2012-04-12 to UT 2012-07-09. The spectra have a resolving power of $R=44,000$, and were extracted following the procedures described by Buchhave et al. (2010). These three initial TRES single-order absolute RVs are listed in Table 1 and are consistent with no RV variations to within the errors, ruling out some classes of astrophysical false positives. However, the TRES RV uncertainties are large enough to still allow for a low-mass companion at the ~ 7.8 d period of the KELT-North candidate signal, and on that basis we chose to continue with photometric follow-up. Note that due to the relatively large uncertainties, we chose not to include these TRES velocities in the final global analysis described in §4.

On UT 2012-06-26, we obtained high precision KELT-6 follow-up photometry of the final third of a predicted transit and detected an apparent shallow egress (see §2.3). Based on that detection and the lack of RV variations in the TRES data, we decided to pursue higher-precision RV data.

Using the High Resolution Echelle Spectrometer (HIRES) instrument (Vogt et al. 1994) on the Keck I telescope located on Mauna Kea, Hawaii, we obtained 16 exposures between UT 2012-08-24 and UT 2013-02-21 with an iodine cell, plus a single iodine-free template spectrum. The absolute and precise relative RV measurements are listed in Table 1, and Figure 2 shows the HIRES relative RV data phased to the orbit fit with a linear trend of $\dot{\gamma} = -0.239 \text{ m s}^{-1} \text{ day}^{-1}$ (see §4) removed, along with the residuals to the model fit.

The HIRES radial velocity observations were made using the standard setup of the California Planet Search (CPS) program (Johnson et al. 2010; Howard et al. 2011). A pyrex cell containing gaseous iodine is placed in front of the spectrometer entrance slit, which imprints a dense set of molecular iodine lines on each stellar spectrum. The iodine lines provide a calibration of the instrumental profile as well as a precise measure of the wavelength scale at the time of observation (Marcy & Butler 1992). We measured the relative stellar radial velocities using the forward-modeling scheme of Butler et al. (1996) with improvements made over the years. We measured the absolute RVs using the methods of Chubak et al. (2012).

The PSF varies quite dramatically in the slit-fed HIRES instrument simply from guiding and spectrometer focus variations. Since line asymmetries due to instrumental and stellar sources cannot be easily distinguished, we do not attempt to measure bisector spans for the HIRES observations.

We also obtained five RV measurements between UT 2013-02-01 and UT 2013-02-15 using the Hobby-Eberly Telescope (HET). However, these data were taken without an iodine cell for wavelength reference, and as a result the uncertainties are $>6 \text{ km s}^{-1}$, so we do not list them in the RV table or use them in the global fit analysis in §4.

Finally, 21 additional TRES RVs were obtained and reduced using multi-order analysis after most of the global analysis had been completed. The full TRES RV dataset is listed in Table 1 and contains measurements from 24 different nights between UT 2012-04-12 and UT 2013-07-31, with typical relative uncertainties of 20 m s^{-1} . Although we do not use the TRES RV data in our global fit analysis (see §4.2), we note

Table 1
Radial Velocity and Bisector Span Variation Measurements of KELT-6

BJD _{TDB}	Abs RV ^a	Rel RV ^b	Rel σ_{RV} ^c	BS ^d	σ_{BS} ^e	Source
2456029.869867	1085	27.02	20.27	-3.9	21.6	TRES
2456114.681684	1188	-5.96	28.33	-18.0	19.0	TRES
2456117.673406	1166	63.43	19.73	17.3	14.4	TRES
2456163.733467	1300	19.38	3.90	-	-	HIRES
2456164.729771	1216	61.75	3.76	-	-	HIRES
2456165.727060	1202	46.70	3.76	-	-	HIRES
2456172.720200	1209	64.03	3.36	-	-	HIRES
2456173.720971	1163	69.62	3.31	-	-	HIRES
2456175.727980	1081	-5.05	5.06	-	-	HIRES
2456177.719323	1161	-14.71	3.56	-	-	HIRES
2456178.716548	1000	2.82	3.57	-	-	HIRES
2456179.715151	1214	43.05	3.67	-	-	HIRES
2456290.173359	1311	29.64	3.81	-	-	HIRES
2456318.978815	1132	-46.73	3.50	-	-	HIRES
2456320.088103	1319	-35.17	3.48	-	-	HIRES
2456326.175000	1185	-62.66	3.50	-	-	HIRES
2456327.103147	1340	-49.24	3.52	-	-	HIRES
2456328.106726	1333	-11.70	3.32	-	-	HIRES
2456345.026477	1291	8.71	3.58	-	-	HIRES
2456443.707006	1109	-33.79	22.37	7.4	13.4	TRES
2456450.707562	1125	-18.64	19.40	-8.2	15.4	TRES
2456451.710411	1021	-54.28	19.92	-0.2	15.3	TRES
2456452.667049	1022	-79.97	17.75	0.5	10.2	TRES
2456453.661056	1044	16.31	21.20	-50.3	18.9	TRES
2456458.688259	1015	-71.18	18.35	8.5	10.8	TRES
2456459.685632	1147	-54.01	17.19	16.6	11.0	TRES
2456460.684562	1022	-57.04	20.36	6.1	10.1	TRES
2456461.669084	1127	-30.88	18.32	11.8	11.6	TRES
2456462.673881	1181	0.00	14.42	5.2	9.0	TRES
2456463.673604	1150	19.16	15.25	12.8	11.2	TRES
2456464.684882	1141	10.16	14.42	1.9	13.9	TRES
2456466.733703	1045	-69.70	17.79	-18.7	13.2	TRES
2456467.707369	1089	-66.40	24.43	-5.8	11.4	TRES
2456468.720609	1071	-78.93	24.46	-13.3	11.2	TRES
2456469.719214	1080	-36.11	22.32	6.0	10.1	TRES
2456470.658849	1168	34.53	19.41	-4.3	9.8	TRES
2456472.704518	1211	-11.86	25.12	30.9	22.1	TRES
2456501.663546	1628	-20.17	33.33	0.5	12.2	TRES
2456503.653861	1697	58.79	33.22	5.4	11.6	TRES
2456504.645862	1577	-2.35	19.21	-8.3	10.8	TRES

Note. — Absolute RVs are on the IAU scale. Based on extensive observations of radial velocity reference stars, the native absolute velocity scale of TRES has been transformed to the IAU absolute velocity scale by subtracting 610 m s^{-1} . The absolute RV error is 100 m s^{-1} and is dominated by the long-term RMS for velocity standard stars. The relative RV values reported are on the native system for each instrument and cannot be directly compared to values from a different instrument. The bisector spans (BS) from the TRES spectra are computed as described in the text.

^aabsolute RVs (m s^{-1})

^brelative RVs (m s^{-1})

^cunrescaled relative RV errors (m s^{-1})

^dspectral line bisector spans (m s^{-1})

^espectral line bisector span errors (m s^{-1})

that these data independently confirm both the amplitude of the KELT-6b RV variations (see Figure 2) and the linear trend of the fiducial global fit (see §5), albeit with larger uncertainties due to the somewhat worse precision than the Keck data. Bisector spans were calculated from the TRES spectra following Torres et al. (2007) and are used in §6 as part of the false positive analysis. The bisector spans are listed in Table 1, and shown in the bottom panel of Figure 2 phased to the orbital fit.

²⁸ <http://tdc-www.harvard.edu/instruments/tres/>

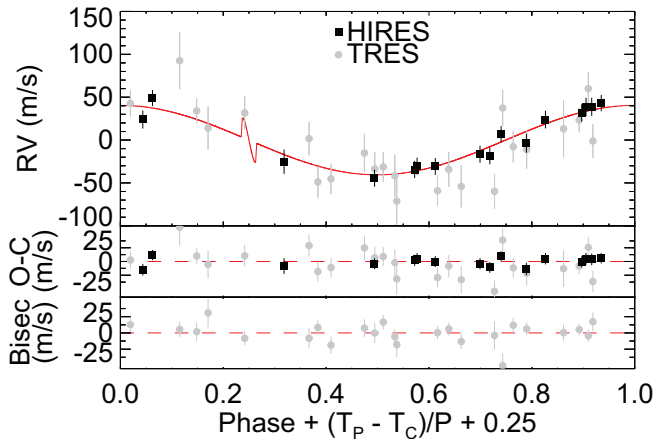


Figure 2. Hires and TRES relative radial velocity measurements of KELT-6. *Top panel:* Relative RV observations phased to our fiducial orbital model (see §4.2) which is fit to the Hires data only with eccentricity and the RV linear trend as free parameters. The fiducial model is shown as a solid red line. The predicted Rossiter-McLaughlin effect incorporates an assumption that $\lambda = 0$ (i.e. that the projected spin-orbit alignment of the system is 0 degrees). Hires observations are shown as black squares and the error bars are scaled according to the method described in §4. TRES observations are shown as gray circles with unrescaled errors. These data were not used in the fit, but are simply phased to the period of the fiducial model, and shifted by a constant offset that minimizes the χ^2 of the data from the fiducial model. *Middle panel:* Residuals of the RV observations to the fiducial fit. The RMS of the Hires RV residuals is 8.0 m s^{-1} . *Bottom panel:* Bisector spans of the TRES spectra.

2.3. Follow-up Time-Series Photometry

We acquired follow-up time-series photometry of KELT-6 to check for other types of false positives and to better determine the transit shape. To schedule follow-up photometry, we used the *Tapir* software package (Jensen 2013). We obtained 16 partial or full primary transits in multiple bands between June 2012 and June 2013. The transit duration (> 5.5 hours) and orbital period (> 7.8 days) are long, so opportunities to observe full transits are rare. Figure 3 shows all the primary transit follow-up light curves assembled. A summary of the follow-up photometric observations is shown in Table 2. We find consistent R_P/R_* ratios in all light curves, which include observations in the g , r , i , z , V , I , and CBB filters²⁹, helping to rule out false positives due to blended eclipsing binaries. Figure 4 shows all primary transit follow-up light curves from Figure 3 (except the WCO light curve which contains significant residual systematics after detrending), combined and binned in 5 minute intervals. This combined and binned light curve is not used for analysis, but rather to show the best combined behavior of the transit. We also observed KELT-6 near the uncertain time of secondary transit on five different epochs (see §6).

Unless otherwise noted, all photometric follow-up observations were reduced with the *AstroImageJ* (AIJ) package³⁰ (K. A. Collins & J. F. Kielkopf 2014, in preparation). AIJ is a general purpose image processing package, but is optimized for processing time-series astronomical image sequences. It is open source software written in Java and is compatible

²⁹ In all references to SDSS filters in this paper, we use the unprimed notation to denote generic SDSS-like filters, which in practice are often labeled with the primed notation. CBB denotes the Astrodon clear with blue block filter which starts transmitting near 500 nm and continues to transmit into the near-infrared.

³⁰ <http://www.astro.louisville.edu/software/astroimagej/>

with all computing platforms commonly used to process astronomical data. AIJ is a graphical user interface driven package that provides an interactive multi-image display interface, CCD image calibration (bias, dark, flat-field, and non-linearity correction), astronomical time and coordinate calculations, multi-aperture differential photometry, multi-dataset plotting, and interactive light curve detrending. It can be operated in combination with any camera control software to reduce data and plot differential light curves in real time, or can be used in standard mode to post process data.

Also unless otherwise noted, calibration of all photometric follow-up observations included bias and dark subtraction followed by flat-field correction. Calibration of the MORC data also included a correction for CCD non-linearity. Differential photometry was performed on the calibrated images using a circular aperture.

We observed three complete and three partial transits of KELT-6 using two telescopes at Moore Observatory, operated by the University of Louisville. The 0.6 m RCOS telescope with an Apogee U16M $4K \times 4K$ CCD, giving a $26' \times 26'$ field of view and $0.39 \text{ arcseconds pixel}^{-1}$, was used to observe the r egress on UT 2012-06-26, the r ingress on UT 2012-12-23, the full r transit on UT 2013-02-24, the z egress on UT 2013-03-04, and the full r transit on UT 2013-04-20. The 0.6 m was also used to observe near the time of secondary transit on UT 2013-04-16 in z . The Planewave Instruments 0.5 m CDK telescope with an Apogee U16M $4K \times 4K$ CCD, giving a $37' \times 37'$ field of view and $0.54 \text{ arcseconds pixel}^{-1}$, was used to observe most of a transit in g on UT 2013-02-24. The gap in the data is due to a meridian flip.

We observed an egress in g at Swarthmore College's Peter van de Kamp Observatory on UT 2013-01-08. The observatory uses a 0.6 m RCOS telescope with an Apogee U16M $4K \times 4K$ CCD, giving a $26' \times 26'$ field of view. Using 2×2 binning, it has $0.76 \text{ arcseconds pixel}^{-1}$.

We observed one partial and two full transits at Spot Observatory. The observatory uses a 0.6 m RCOS telescope with an SBIG STX 16803 $4K \times 4K$ CCD, giving a $26' \times 26'$ field of view and $0.39 \text{ arcseconds pixel}^{-1}$. An ingress in i was observed on UT 2013-02-16, and full transits were observed on UT 2013-02-24 in i and UT 2013-04-20 in z . We also observed near the time of secondary transit on UT 2013-02-20 in z .

We observed an egress in z on UT 2013-02-24 and an ingress in i on UT 2013-06-06 with KeplerCam on the 1.2 m telescope at FLWO. KeplerCam has a single $4K \times 4K$ Fairchild CCD with $0.366 \text{ arcseconds pixel}^{-1}$, and a field of view of $23.1' \times 23.1'$. We also observed near the time of secondary transit on UT 2013-02-28, UT 2013-04-08, and UT 2013-04-24 in z .

We observed one full and one partial transit at Montgomery Bell Academy (MBA) Long Mountain Observatory. The observatory uses a PlaneWave Instruments 0.6 m CDK telescope with an SBIG STL 11002 4008×2672 CCD, giving a $30' \times 20'$ field of view and $0.45 \text{ arcseconds pixel}^{-1}$. A full transit was observed in V on UT 2013-02-24. However, the resulting light curve had large systematics that we were unable to adequately remove. Since the same transit epoch was observed by both Moore Observatory telescopes in overlapping filter bands, these data added no new information to the analysis and was not included in the global fit described in §4. An egress in I was observed on UT 2013-03-04, and observations near the time of secondary transit were collected in z on UT

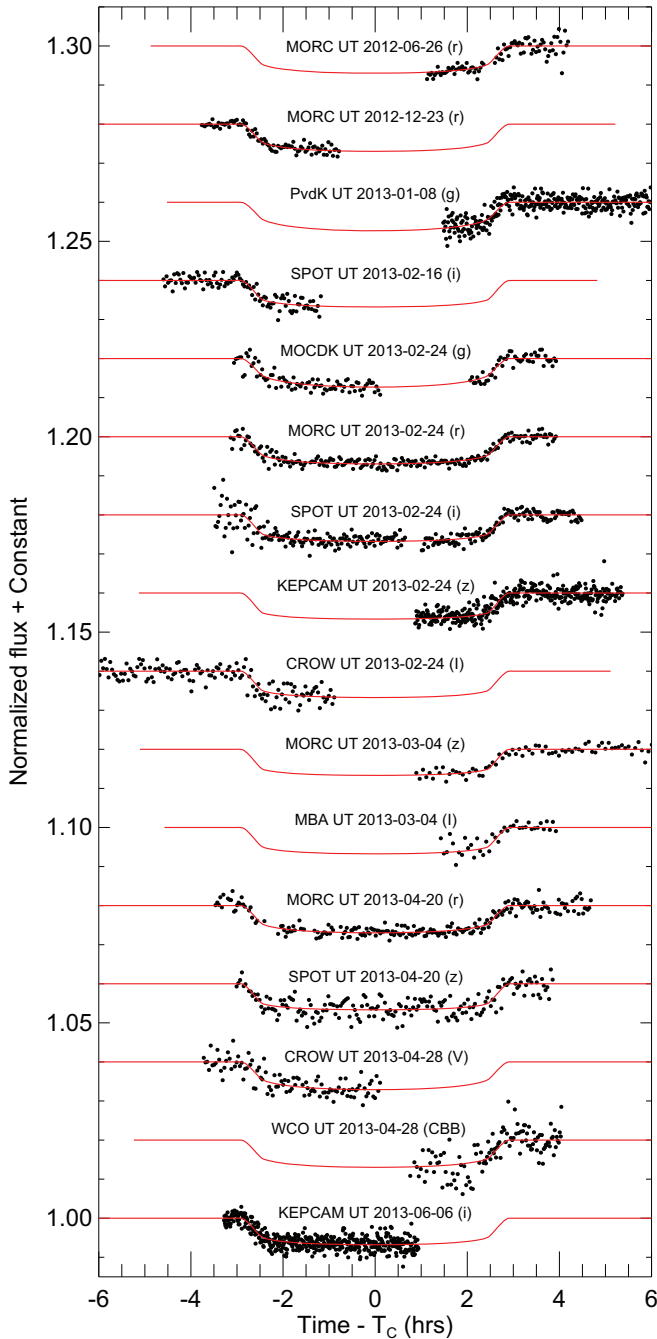


Figure 3. Follow-up transit photometry of KELT-6. The red overplotted lines are the best fit transit model from global fit 6 described in §4.2 and summarized in Table 5. The transit times are shown in Table 3. The labels are as follows: MORC=University of Louisville Moore Observatory 0.6 m RCOS Telescope; PvdKO=Peter van de Kamp Observatory 0.6 m RCOS Telescope; SPOT=Spot Observatory 0.6 m RCOS Telescope; MOC DK=University of Louisville Moore Observatory PlaneWave 0.5 m CDK Telescope; KEPCAM=KeplerCam at the Fred Lawrence Whipple Observatory 1.2 m Telescope; CROW=Canela’s Robotic Observatory 0.3 m LX200 Telescope; MBA=Montgomery Bell Academy 0.6 m PlaneWave CDK Telescope; WCO=Westminster College Observatory 0.35 m C14 Telescope.

2013-02-20.

We observed two partial transits at Canela’s Robotic Observatory (CROW) in Portugal. The observations were obtained using a 0.3 m LX200 telescope with an SBIG ST-8XME 1530

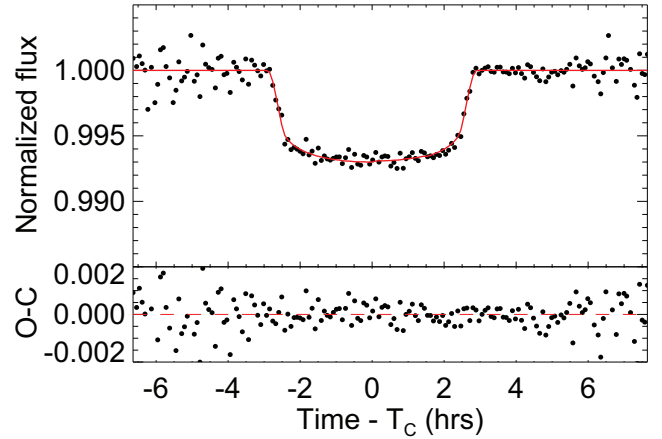


Figure 4. *Top panel:* All follow-up light curves from Figure 3 (except the WCO light curve - see text), combined and binned in 5 minute intervals. This light curve is not used for analysis, but rather to show the best combined behavior of the transit. The red curve shows the 15 transit models from global fit 6 described in Table 5 for each of the individual fits combined and binned in 5 minute intervals the same way as the data, with the model points connected. *Bottom panel:* The residuals of the binned light curve from the binned model in the top panel.

$\times 1020$ CCD, giving a $28' \times 19'$ field of view and 1.11 arcseconds pixel^{-1} . An ingress was observed in I_c on UT 2013-02-24, and an ingress was observed in V on UT 2013-04-28.

We observed a partial transit at Westminster College Observatory (WCO) in Pennsylvania. The observations were obtained using a Celestron 0.35 m C14 telescope with an SBIG STL-6303E 3072×2048 CCD, giving a $24' \times 16'$ field of view and 1.4 arcseconds pixel^{-1} at 3×3 pixel binning. An egress was observed using an Astrodon Clear with Blue Blocking (CBB) filter on UT 2013-04-28.

We observed near the time of secondary transit on UT 2013-04-08 and UT 2013-04-24 using the 1.0 m telescope at the ELP node of the Las Cumbres Observatory Global Telescope (LCOGT) network at McDonald observatory in Texas (Brown et al. 2013). The observations were obtained in the Pan-STARRS-Z band with an SBIG STX-16803 4096×4096 CCD, giving a $15.8' \times 15.8'$ field of view and 0.464 arcseconds pixel^{-1} (2×2 binning). The ELP data were processed using the pipeline discussed in Brown et al. (2013).

2.4. Adaptive Optics Observations

We obtained adaptive optics (AO) imaging using NIRC2 (instrument PI: Keith Matthews) at Keck on UT 2012-12-07. The AO imaging places limits on the existence of nearby eclipsing binaries that could be blended with the primary star KELT-6 at the resolution of the KELT and follow-up data, thereby causing a false positive planet detection. In addition, it places limits on any nearby blended source that could contribute to the total flux, and thereby result in an underestimate of the transit depth and thus planet radius in the global fit presented in §4. Our observations consist of dithered frames taken with the K' filter. We used the narrow camera setting to provide fine spatial sampling of the stellar point-spread function, and used KELT-6 as its own on-axis natural guide star. The total on-source integration time was 225 seconds. The resulting image is shown in Figure 5.

We find no significant detection of off-axis sources in the immediate vicinity of KELT-6. We note that there are some conspicuous sources at the threshold of detection. However, without an image in a different filter, we are unable to de-

Table 2
Summary of Photometric Observations

Telescope	UT Date	# Obs	Band	Cycle ^a (sec)	RMS ^b (10 ⁻³)	PNR ^c ($\frac{10^{-3}}{\text{minute}}$)	Detrend Variables
Primary:							
MORC	2012-06-26	87	<i>r</i>	119	1.6	2.3	AM
MORC	2012-12-23	91	<i>r</i>	119	0.8	1.1	AM
PvdKO	2013-01-08	315	<i>g</i>	52	1.7	1.6	AM,PK
SPOT	2013-02-16	104	<i>i</i>	119	1.4	2.0	AM,TM
MOC DK	2013-02-24	131	<i>g</i>	141	1.3	2.0	AM,MF,SK
MORC	2013-02-24	212	<i>r</i>	119	1.0	1.4	AM,FW
SPOT	2013-02-24	278	<i>i</i>	99	1.8	2.3	AM,MF
KEPCAM	2013-02-24	361	<i>z</i>	45	1.6	1.4	AM,SK
CROW	2013-02-24	148	<i>I</i>	142	1.9	2.9	AM,PK,TM
MORC	2013-03-04	95	<i>z</i>	259	1.0	2.1	AM,TM
MBA	2013-03-04	39	<i>I</i>	236	1.5	3.0	AM
MORC	2013-04-20	212	<i>r</i>	119	1.2	1.7	AM
SPOT	2013-04-20	179	<i>z</i>	139	2.0	3.0	AM,TM
CROW	2013-04-28	102	<i>V</i>	135	2.1	3.2	AM,MF
WCO	2013-04-28	114	<i>CBB</i>	105	3.0	4.0	AM,TM
KEPCAM	2013-06-06	441	<i>i</i>	35	1.6	1.2	AM
Secondary:							
MBA	2013-02-20	58	<i>z</i>	236	1.5	3.0	AM
SPOT	2013-02-20	47	<i>z</i>	259	1.3	2.7	AM
KEPCAM	2013-02-28	757	<i>z</i>	35	2.0	1.5	AM
KEPCAM	2013-04-08	324	<i>z</i>	45	1.7	1.5	AM,XY
ELP	2013-04-08	162	<i>PS-Z</i>	90	1.9	2.3	AM,XY
MORC	2013-04-16	72	<i>z</i>	259	1.4	2.9	AM
ELP	2013-04-24	204	<i>PS-Z</i>	90	2.5	3.1	AM,XY
KEPCAM	2013-04-24	701	<i>z</i>	35	2.4	1.8	AM

Note. — MORC=University of Louisville Moore Observatory 0.6 m RCOS Telescope; PvdKO=Peter van de Kamp Observatory 0.6 m RCOS Telescope; SPOT=Spot Observatory 0.6 m RCOS Telescope; MOC DK=University of Louisville Moore Observatory PlaneWave 0.5 m CDK Telescope; KEPCAM=KeplerCam at the Fred Lawrence Whipple Observatory 1.2 m Telescope; CROW=Canela’s Robotic Observatory 0.3 m LX200 Telescope; MBA=Montgomery Bell Academy 0.6 m PlaneWave CDK Telescope; WCO=Westminster College Observatory 0.35 m C14 Telescope; ELP=McDonald 1.0 m Telescope (Las Cumbres Observatory Global Telescope Network); AM=airmass; PK=peak count in aperture; TM=time; MF=meridian flip; SK=sky background; FW=average FWHM in image; XY=detector x,y coordinates of target star centroid; PS-Z=Pan-STARRS-Z.

^aCycle time in seconds, calculated as the mean of exposure time plus dead time during periods of back-to-back exposures.

^bRMS of residuals from the best fit model in units of 10⁻³.

^cPhotometric noise rate in units of 10⁻³ minute⁻¹, calculated as $\text{RMS}/\sqrt{\Gamma}$, where RMS is the scatter in the light curve residuals and Γ is the mean number of cycles (exposure time and dead time) per minute during periods of back-to-back exposures (adapted from Fulton et al. 2011).

termine if the position of these sources are wavelength dependent, which would indicate that they are speckles rather than real sources. Nevertheless, we can still place a conservative upper limit on any real sources based on the contrast sensitivity. Figure 6 shows the 10 σ contrast sensitivity (in Δ magnitude) versus angular separation computed from Figure 5 using a three-point dither pattern to build signal and subtract sky-background (see Crepp et al. 2012). The top scale in Figure 6 shows projected separation in AU for a distance of 222 pc (see Table 4). The scale on the right side of the plot estimates the mass in units of M_{\odot} at a given contrast, estimated using the Baraffe et al. (1998) models. We can exclude companions beyond a distance of 0.5 arcseconds (111 AU) from KELT-6 down to a magnitude difference of 6.0 magnitudes at 10 σ .

3. HOST STAR PROPERTIES

3.1. Properties from the Literature

Table 4 lists various properties and measurements of KELT-6 collected from the literature and derived in this work. The

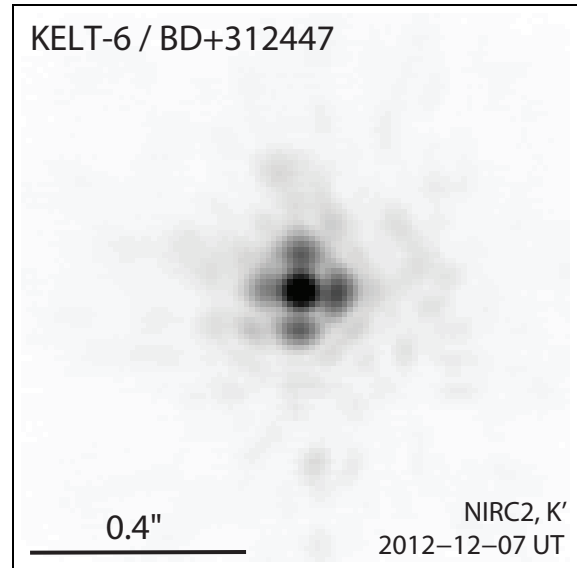


Figure 5. Keck adaptive optics image of KELT-6 taken with NIRC2 in the K’ filter. The image is displayed on a negative square-root intensity scale to emphasize the surrounding regions. North is up, and east is left.

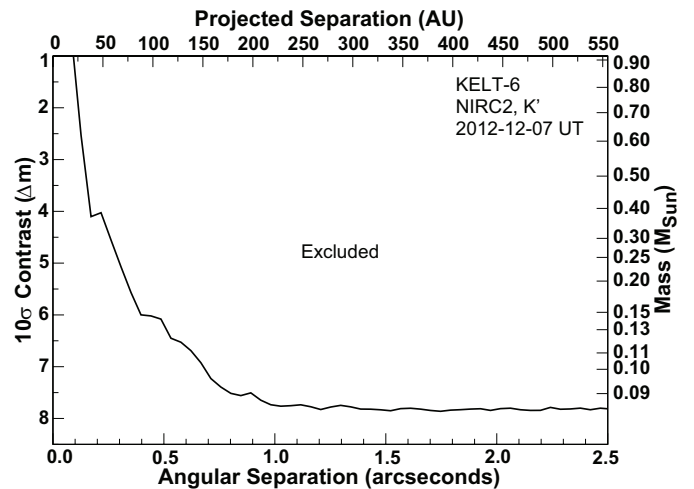


Figure 6. Contrast sensitivity derived from the Keck adaptive optics image of KELT-6 shown in Figure 5. The 10 σ contrast in Δ magnitude is plotted against angular separation in arcseconds. The scale on top shows projected separation in AU for a distance of 222 pc (see Table 4). The scale on the right side of the plot estimates the mass in units of M_{\odot} at a given contrast, estimated using the Baraffe et al. (1998) models. We can exclude companions beyond a distance of 0.5 arcseconds (111 AU) from KELT-6 down to a magnitude difference of 6.0 magnitudes at 10 σ .

data from the literature include FUV and NUV fluxes from GALEX (Martin et al. 2005), $B-V$ color from Harris & Uppgren (1964), optical fluxes in the B_T and V_T passbands from the Tycho-2 catalog (Høg et al. 2000), V and I_C from The Amateur Sky Survey (TASS; Richmond et al. 2000), near-infrared (IR) fluxes in the J , H and K_S passbands from the 2MASS Point Source Catalog (Skrutskie et al. 2006; Cutri et al. 2003), near- and mid-IR fluxes in three WISE passbands (Wright et al. 2010; Cutri et al. 2012), and proper motions from the NOMAD catalog (Zacharias et al. 2004).

3.2. Spectroscopic Analysis

We use both the TRES and HIRES spectra to derive the stellar properties of KELT-6. To analyze the TRES spectra, we use the Spectral Parameter Classification (SPC) procedure version 2.2 (Buchhave et al. 2012) with T_{eff} , $\log g_*$, $[\text{M}/\text{H}]$, and $v \sin i_*$ as free parameters. Since each of the 24 TRES spectra yielded similar results, we took the mean value for each stellar parameter. The uncertainties are dominated by systematic rather than statistical errors, so we adopt the mean error for each parameter. The results are: $T_{\text{eff}} = 6098 \pm 50$ K, $\log g_* = 3.83 \pm 0.10$, $[\text{M}/\text{H}] = -0.34 \pm 0.08$, and $v \sin i_* = 6.7 \pm 0.5$ km s $^{-1}$, giving the star an inferred spectral type of F8.

To analyze the HIRES spectra, we use spectral synthesis modeling with Spectroscopy Made Easy (SME, Valenti & Piskunov 1996, Valenti & Fischer 2005). The free parameters for the model included T_{eff} , $v \sin i_*$, $\log g_*$, and $[\text{Fe}/\text{H}]$. The microturbulent velocity was fixed to 0.85 km s $^{-1}$ in this model and the macroturbulent velocity was specified as a function of effective temperature (Valenti & Fischer 2005). After the first model was generated, two other iterations were run with temperature offsets of ± 100 K from the model temperature to evaluate degeneracy between the model parameters. If the RMS for these new fit parameters relative to the original model values exceeds the uncertainties on the original model values estimated using the error analysis of Valenti & Fischer (2005), then these larger uncertainties are adopted. However, in this case, the fits starting with the temperature offsets settled on values very close to those found using the original model, differing by much less than the estimated uncertainties on the original model values. Therefore, we adopted these original uncertainties, which include systematic error sources as described in Valenti & Fischer (2005). Based on this analysis, KELT-6 appears to be a main sequence or very slightly evolved subgiant with $T_{\text{eff}} = 6100 \pm 44$ K, $\log g_* = 3.961 \pm 0.060$ and sub-solar metallicity, $[\text{Fe}/\text{H}] = -0.277$. The star has a projected rotational velocity $v \sin i_* = 5.0 \pm 0.5$ km s $^{-1}$.

Comparing the parameter values determined from the TRES spectra using SPC v2.2 to those determined from the HIRES spectra using SME, we generally find agreement to $\sim 1\sigma$ or better, except for $v \sin i_*$, which differs by $\sim 3\sigma$. We do not have a good explanation for the $v \sin i_*$ discrepancy. However, we do not use $v \sin i_*$ in our global fits, so this discrepancy is unimportant for the present analysis. The individual TRES spectra have a signal-to-noise ratio (SNR) of ~ 40 while the HIRES spectrum used to derive the stellar parameters has a SNR of ~ 180 . We therefore adopt the higher SNR HIRES stellar parameters for the analyses in this paper, although we note that the uncertainties in both determinations are likely to be dominated by systematic errors.

3.3. UVW Space Motion

We evaluate the motion of KELT-6 through the Galaxy to place it among standard stellar populations. We adopt an absolute radial velocity of $+1.1 \pm 0.2$ km s $^{-1}$, based on the mean of the TRES and HIRES absolute RVs listed in Table 1, where the uncertainty is due to the systematic uncertainties in the absolute velocities of the RV standard stars. Combining the adopted absolute RV with distance estimated from fitting the spectral energy distribution (§3.4) and proper motion information from the NOMAD catalog (Zacharias et al. 2004), we find that KELT-6 has U, V, W space motion (where positive U is in the direction of the Galactic Center) of -6.3 ± 0.9 ,

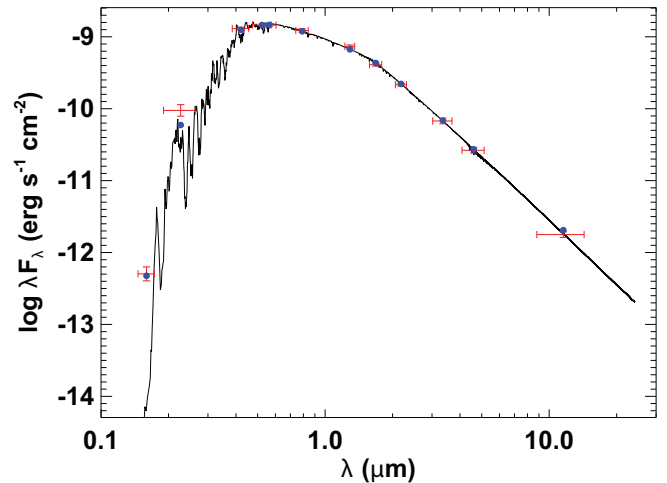


Figure 7. Measured and best-fit SED for KELT-6 from UV through mid-IR. The intersection points of the red error bars indicate measurements of the flux of KELT-6 in the UV, optical, NIR, and mid-IR passbands listed in Table 4. The vertical error bars are the 1σ photometric uncertainties, whereas the horizontal error bars are the effective widths of the passbands. The solid curve is the best-fit theoretical SED from the NextGen models of Hauschildt et al. (1999), assuming stellar parameters T_{eff} , $\log g_*$ and $[\text{Fe}/\text{H}]$ fixed at the values in Table 6 from the fiducial fit, with A_V and d allowed to vary. The blue dots are the predicted passband-integrated fluxes of the best-fit theoretical SED corresponding to our observed photometric bands.

23.2 ± 0.8 , 6.9 ± 0.2 , all in units of km s $^{-1}$, making it unambiguously a thin disk star.

3.4. SED Analysis

We construct an empirical, broad-band spectral energy distribution (SED) of KELT-6, shown in Figure 7. We use the FUV and NUV fluxes from GALEX (Martin et al. 2005), the B_T and V_T colors from the Tycho-2 catalog (Høg et al. 2000), V and I_C from TASS (Richmond et al. 2000), near-infrared (NIR) fluxes in the J , H , and K_S passbands from the 2MASS Point Source Catalog (Cutri et al. 2003; Skrutskie et al. 2006), and the near- and mid-IR fluxes in three WISE passbands (Wright et al. 2010). We fit this SED to NextGen models from Hauschildt et al. (1999) by fixing the values of T_{eff} , $\log g_*$ and $[\text{Fe}/\text{H}]$ inferred from the fiducial model fit to the light curve, RV, and spectroscopic data as described in §4 and listed in Table 6, and then finding the values of the visual extinction A_V and distance d that minimize χ^2 . The best fit model has a reduced χ^2 of 1.61 for 10 degrees of freedom. We find $A_V = 0.01 \pm 0.02$ and $d = 222 \pm 8$ pc. We note that the quoted statistical uncertainties on A_V and d are likely to be underestimated because we have not accounted for the uncertainties in values of T_{eff} , $\log g_*$ and $[\text{Fe}/\text{H}]$ used to derive the model SED. Furthermore, it is likely that alternate model atmospheres would predict somewhat different SEDs and thus values of the extinction and distance.

4. CHARACTERIZATION OF THE SYSTEM

To determine the final orbital and physical parameters of the KELT-6 system, we combine the results from the spectroscopic analysis, the light curves, and the HIRES RVs of KELT-6 as inputs to a global fit using a custom version of EXOFAST (Eastman et al. 2013). The TRES RVs are not used in the global fit analysis. The EXOFAST analysis package does a simultaneous Markov Chain Monte Carlo (MCMC) fit to the photometric and spectroscopic data to derive system parameters. It includes constraints on the stellar parameters M_* and

R_* from either the empirical relations in Torres et al. (2010) or from Yonsei-Yale stellar models (Demarque et al. 2004), in order to break the well-known degeneracy between M_* and R_* for single-lined spectroscopic eclipsing systems. EXOFAST scales the RV and light curve data uncertainties such that the probability that the χ^2 is larger than the value we achieved, $P(> \chi^2)$, is 0.5, to ensure the resulting parameter uncertainties are roughly accurate. The global fit method is similar to that described in detail in Siverd et al. (2012), but we note a few differences below.³¹

4.1. Light Curve Detrending

Because KELT-6b’s transits have an unusually long duration and relatively shallow depth (by ground-based observing standards), treatment of light curve systematics plays an important role in the accuracy of parameters determined by the EXOFAST global fit. The inclusion of detrending parameters into the global fit can often mitigate the effect of light curve systematics, but sometimes at the expense of introducing extra local minima in χ^2 space, which may cause other complications in the analysis. Therefore, it is important to maximize the detrending improvements to the fit of each light curve while minimizing the number of detrending parameters.

Systematically fitting each light curve using all combinations of ~ 15 possible detrending parameters and comparing all of the resulting χ^2 values using the $\Delta\chi^2$ statistic would be prohibitive. Instead, we opted to use the interactive detrending capabilities of the AIJ package (see §2.3) to search for up to three parameters that appeared to reduce the systematics in each light curve. We then individually fit each of the full transit light curves using EXOFAST, and repeated the fit using various combinations of the detrending parameters selected for that light curve. Finally, we compared χ^2 from before and after the inclusion of an additional detrending parameter to determine if the probability of a chance improvement was more than a few percent. If so, we did not include the additional detrending parameter in the global fit.

It is important to emphasize that the light curves fitted in EXOFAST were the raw light curves (i.e. not the detrended light curves from AIJ). The only way in which the results of the AIJ analysis entered into the final analysis was in the choice of detrending parameters and the initial conditions adopted. Specifically, the detrend parameter coefficients determined in AIJ were used as starting points for the EXOFAST fits. However these parameter coefficients were otherwise allowed to vary freely in order to minimize χ^2 .

One detrending parameter we included that warrants additional discussion is an offset in the zero point of the photometry arising from a change in placement of the target and/or comparison star(s) on the CCD pixel array during time series observations. These positional changes typically result in a zero point shift in the photometry at that epoch in the light curve due to interpixel response differences and imperfect flat-field corrections. We found such positional changes due to a meridian flip in the MOCCK light curve on UT 2013-02-24, as well as an equipment failure in the SPOT UT 2013-

02-24 light curve (see Table 2 and Figure 3). We therefore included a detrending parameter that accounts for a change in the zero point of the relative photometry before and after the specified time.

In addition, fits to individual partial light curves often resulted in obviously incorrect models. We therefore chose detrending parameters for such ingress- or egress-only data by hand using AIJ without a rigorous $\Delta\chi^2$ analysis.

Light curves from near the time of predicted secondary eclipse were treated somewhat differently. In particular, these were airmass detrended directly in AIJ, and when abrupt changes in the light curve were correlated with a change in position of the target star on the detector, x and y pixel positions of the target star centroid were also used as detrending parameters.

The final detrending parameters adopted for all of the light curves are shown in Table 2.

4.2. Global Fits

Using the KELT-6b primary transit light curves, the detrending parameters and priors determined in the previous section, and the results from the HIRES RV and spectroscopic analyses, we computed a series of 12 global fits using our custom version of EXOFAST. The results of six illustrative global fits are shown in Table 5. The table lists four global fit parameter choices (as detailed in the remainder of this subsection) for each of the six fits, along with the values of several key system parameters computed as part of each fit.

All global fits included a prior on orbital period $P = 7.8457 \pm 0.0002$ days from the KELT-North data and priors on host star effective temperature $T_{\text{eff}} = 6100 \pm 44$ K and metallicity $[\text{Fe}/\text{H}] = -0.277 \pm 0.04$ from the HIRES spectroscopy. The priors were implemented as a χ^2 penalty in EXOFAST (see Eastman et al. 2013 for details). For some of the global fits we also included a prior on stellar surface gravity $\log g_* = 3.961 \pm 0.060$ from the HIRES spectroscopy. For the others, $\log g_*$ was constrained only by the transit data through the well-known direct constraint on ρ_* from the light curve and RV data, combined with a constraint on the stellar mass-radius relation through either the Torres relations or the Yonsei-Yale evolutionary models. Fitting the HIRES RV data independently to a Keplerian model, we found an acceleration (“RV slope”) of $-0.239 \text{ m s}^{-1} \text{ day}^{-1}$, which is highly significant at the $\sim 7\sigma$ level. Therefore, we proceeded with RV slope as a free parameter for all global fits.

In addition to the slope, there were four additional choices that had to be considered when performing the global fit. First, we needed to decide which transits to include in the global fit. We defined two alternative sets of light curve data to consider: (1) the 5 “full” transits with both an ingress and egress and (2) all 16 full and partial transits. Second, as mentioned previously, we had the option to either include a prior on stellar surface gravity $\log g_* = 3.961 \pm 0.060$ based on the HIRES spectroscopy, or to fit for stellar surface gravity without a prior. Third, we had the option to fit the orbital eccentricity and argument of periastron as free parameters or fix them to zero to force a circular orbit. Fourth, we had the option to break the degeneracy between M_* and R_* by imposing external constraints either from the relations of Torres et al. (2010) (Torres constraints) or by imposing constraints from the Yonsei-Yale stellar models (Demarque et al. 2004) (Yonsei-Yale constraints).

We first computed the four combinations of global fits us-

³¹ In the EXOFAST analysis, which includes the modeling of the filter-specific limb darkening parameters of the transit, we employ the transmission curves defined for the primed SDSS filters rather than the unprimed versions. We also use the Kepler transmission curve to approximate the CBB filter. We expect any differences due to those discrepancies to be well below the precision of all our observations in this paper and of the limb darkening tables from Claret & Bloemen (2011).

ing the 5 full transits with the Torres constraints. The four global fits are defined by the different combinations of eccentric vs. circular orbits, and $\log g_*$ with a spectroscopic prior vs. $\log g_*$ free. The column labeled “Fit 5” in Table 5 shows the results for the Torres constrained, eccentric global fit, with no $\log g_*$ prior. As discussed in §7.1, we plotted Yonsei-Yale stellar evolution tracks corresponding to the stellar mass and metallicity results from these global fits and found that the intersection of $\log g_*$ and T_{eff} values from EXOFAST did not fall within 1σ of the evolutionary tracks. We then computed the four combinations of global fits using the 5 full transits with the Yonsei-Yale constraints and found that for these fits the resulting $\log g_*$ and T_{eff} values were consistent with the corresponding Yonsei-Yale stellar evolution tracks within 1σ error. Parameter values from these four fits are listed in the columns of Table 5 labeled “Fit 1”, “Fit 2”, “Fit 3”, and “Fit 4”. The Torres constrained planet mass and radius are larger than the Yonsei-Yale constrained mass and radius by $\sim 4-7\%$, and although we cannot determine if the Torres relations or the Yonsei-Yale models best represent low metallicity systems, we prefer the Yonsei-Yale constrained global fits for self-consistency with the stellar evolution tracks in §7.1.

We next considered the 16 full and partial transit global fits. We computed only the four combinations corresponding to the adopted Yonsei-Yale constrained global fits. Although we computed very long Markov chains with 10^6 links, three of the four global fits resulted in some parameters (mostly detrending parameters corresponding to partial light curves) that did not fully converge. Converged parameters have greater than 1000 independent draws and a Gelman-Rubin statistic less than 1.01 (see Eastman et al. 2013 and Ford 2006). The column labeled “Fit 6” in Table 5 lists the results for the Yonsei-Yale constrained, eccentric global fit, with no $\log g_*$ prior. The system parameters resulting from the 16 transit global fits are nearly identical to the parameters from the 5 transit global fits. This is to be expected since detrended partial light curves will not add significant constraints to transit depth and shape when jointly fit with full transits. Given the partial transit minor convergence issues, concerns about the ability to properly remove systematics from these light curves, and the lack of significant additional constraints on transit depth and shape from the partial transits, we adopted the global fits based on the 5 full transits. We did however use the 16 transit global fits for the transit timing analysis in §4.3.

Next we examined the adopted Yonsei-Yale constrained global fits that use only the 5 full transits. These four global fits are defined by the different combinations of eccentric vs. circular orbits, and $\log g_*$ prior vs. $\log g_*$ free. Since it is typically difficult to measure $\log g_*$ to the same precision spectroscopically that can be measured from a transit, we choose not to impose a prior on $\log g_*$ from the HIRES spectroscopy. However, we are wary of measurements of $\log g_*$ from the transits in this case, since the duration is very long for a ground-based transit observation. Comparing parameter values in column “Fit 4” of Table 5 with column “Fit 1”, and comparing column “Fit 2” with column “Fit 3”, we found that imposing a spectroscopic prior on $\log g_*$ increased the stellar and planetary radii by $\sim 3\%$ in the circular case and by $\sim 7\%$ in the eccentric case. However, all of the system parameters are within $\sim 1\sigma$ of the results from the global fits without a prior on $\log g_*$.

Since we had no strong prior expectation of tidal circularization of KELT-6b’s relatively long ~ 8 day orbit, we adopted

the more conservative eccentric orbit global fits which have higher parameter errors. The eccentricity resulting from a fit without a spectroscopic prior on $\log g_*$ is $e = 0.22^{+0.12}_{-0.10}$. The eccentricity resulting from a fit with the HIRES spectroscopic prior on $\log g_*$ is $e = 0.27^{+0.11}_{-0.12}$. As pointed out by Lucy & Sweeney (1971), there is a bias for inferred values of eccentricity with low significance, due to the fact that e is a positive definite quantity. Although we adopt an eccentric orbit global fit, we cannot exclude the hypothesis that the orbit of KELT-6b is, in fact, circular.

Our final adopted fiducial stellar and planetary parameters were derived from the 5 full transit, Yonsei-Yale constrained, eccentric orbit global fit with no prior on $\log g_*$. Table 6 lists the full set of system parameters for the fiducial fit.

Comparing the fiducial system parameters with those from the other 11 global fits, we note differences in planetary mass $\Delta M_p \sim 10\%$ ($\sim 1\sigma$), planetary radius $\Delta R_p \sim 10\%$ ($\sim 1\sigma$), orbital radius $\Delta a \sim 5\%$ ($\sim 4\sigma$), planetary equivalent temperature $\Delta T_{\text{eq}} \sim 5\%$ ($\sim 1\sigma$), stellar mass $\Delta M_* \sim 15\%$ ($\sim 3\sigma$), and stellar radius $\Delta R_* \sim 15\%$ ($\sim 1.5\sigma$). Clearly, the choice of global fit input parameters, priors, and external constraints, significantly affects some of the inferred system parameters. Thus, it is important to note that other plausible global fits yield significantly different values for some system parameters.

The HIRES RV uncertainty scaling for the fiducial global fit is 2.808, which is fairly high and is suggestive of substantial stellar jitter in the RV data. The RMS of the RV residuals of the fit to these scaled data is 8.0 m s^{-1} , which is somewhat high ($\sim 2\sigma$) compared to what we would expect based on Wright (2005). We do not have a compelling explanation for the high RV residuals. As noted in §2.2, we did not attempt to measure line bisectors for the HIRES data.

4.3. Transit Timing Variations

We investigated the transit center times of the 16 full and partial transits adopted from the 16 transit, Yonsei-Yale constrained, eccentric orbit global fit with no prior on $\log g_*$ for any signs of transit time variations (TTVs). We were careful to ensure that all quoted times had been properly reported in BJD_{TDB} (e.g., Eastman et al. 2010). When we performed the global fit, we allowed for transit time $T_{C,i}$ for each of the transits shown in Table 3 to be a free parameter. Therefore, the individual follow-up transit light curves do not constrain the KELT-6b ephemeris (global epoch T_C and period P). Rather, the constraints on these parameters in the global fit come only from the RV data, and the prior imposed from the KELT discovery data. Using the follow-up transit light curves to constrain the ephemeris in the global fit would artificially reduce any observed TTV signal.

Subsequent to the global fit, we then derived a separate ephemeris from only the transit timing data by fitting a straight line to all inferred transit center times from the global fit. These times are listed in Table 3 and plotted in Figure 8. We find $T_0 = 2456347.796793 \pm 0.000364$, $P_{\text{Transit}} = 7.8456314 \pm 0.0000459$, with a χ^2 of 38.70 and 14 degrees of freedom. While the χ^2 is larger than one might expect, this is often the case in ground-based TTV studies, likely due to systematics in the transit data. There are $\sim 3\sigma$ deviations from the linear ephemeris on epochs 1 and 8. However, although there are consistent TTV measurements from two independent observatories on both of those epochs, we note that these data are all from ingress or egress only observations.

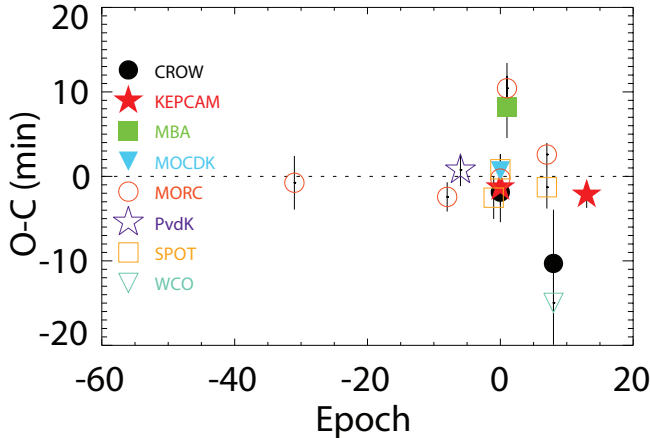


Figure 8. The residuals of the transit times from the best-fit ephemeris. The transit times are given in Table 3. The observatory/telescope abbreviations are the same as in Table 2.

Table 3
KELT-6 Transit Times

Epoch	T_C BJD _{TDB}	σ_{T_C} Sec	O-C Sec	O-C σ_{T_C}	Observatory/ Telescope
-31	2456104.581654	190	-45.17	-0.24	MORC
-8	2456285.030078	104	-145.43	-1.40	MORC
-6	2456300.723507	115	46.31	0.40	PvdKO
-1	2456339.949428	151	-151.18	-1.00	SPOT
0	2456347.797243	118	39.38	0.33	MOCDK
0	2456347.796609	79	-15.31	-0.19	MORC
0	2456347.797368	104	50.44	0.48	SPOT
0	2456347.795916	120	-77.26	-0.64	KEPCAM
0	2456347.795513	213	-112.42	-0.53	CROW
1	2456355.649675	179	625.66	3.48	MORC
1	2456355.648134	220	493.04	2.24	MBA
7	2456402.718026	82	155.28	1.89	MORC
7	2456402.715318	151	-77.39	-0.51	SPOT
8	2456410.554740	381	-618.29	-1.62	CROW
8	2456410.550639	298	-898.14	-3.01	WCO
13	2456449.788514	95	-128.47	-1.35	KEPCAM

Note. — The observatory/telescope abbreviations are the same as in Table 2.

Given the likely difficulty with properly removing systematics in partial transit data, we are unwilling to claim convincing evidence for TTVs. Further study of KELT-6b transit timing is required to rule out TTVs.

5. EVIDENCE FOR A TERTIARY COMPANION

The Keck HIRES radial velocities show a downward trend that is well modeled by a linear slope over the time span of the HIRES RVs as illustrated in Figure 9. The fiducial model, which is displayed as a solid red line, is fit to the HIRES data only and has a slope of $\dot{\gamma} = -0.239 \pm 0.037 \text{ m s}^{-1} \text{ day}^{-1}$. A two-planet fit with the tertiary in a circular orbit yields a negligible improvement of $\Delta\chi^2 = 2.2$ relative to the fit with constant acceleration, which has a $\sim 30\%$ probability of happening by chance. With the inclusion of the full set of 24 reduced TRES RVs (see §2.2) into the single-planet plus slope and two-planet fits, $\Delta\chi^2 = 3.8$, which has a $\sim 15\%$ probability of happening by chance. Although the TRES RVs shown in Figure 9 appear to fairly strongly indicate a turn-over in the RV slope, the statistical analysis above finds only marginal evidence for a turn-over. The TRES RVs shown in Figure 9 have been shifted to best fit the HIRES fiducial model. Characteri-

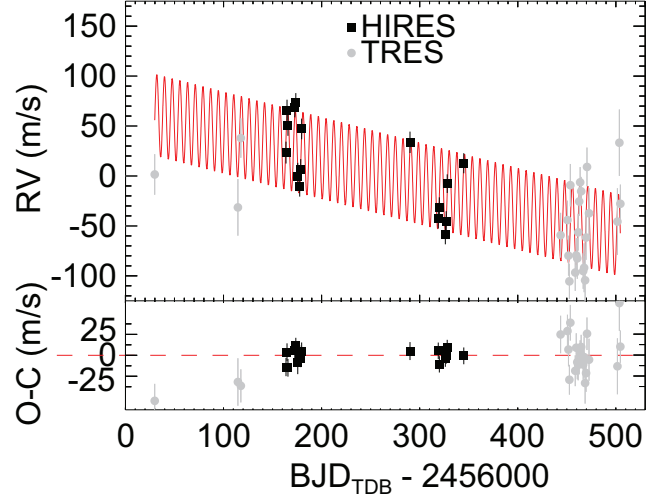


Figure 9. HIRES and TRES unphased KELT-6 radial velocities. HIRES radial velocity measurements are shown as black squares. TRES radial velocities are shown as gray circles. The HIRES error has been scaled by 2.808 as determined by the fiducial EXOFAST global fit (see §4). The TRES errors are unrescaled. The single-planet plus linear slope fiducial model of the KELT-6 system fit to the HIRES data only is shown as a solid red line. The TRES RVs have been shifted by a constant offset that best-fits the fiducial model. Although the TRES data appear to indicate a turnover in the RV slope, a joint fit to the HIRES and TRES data indicate only marginal evidence for a turn-over (see §5).

zation of the tertiary will require continued RV monitoring of the KELT-6 system.

Our Keck AO K' image shows no significant detection of off-axis sources, although there are a couple of speckles at the threshold of detection (see Figure 5 and §2.4). Figure 10 shows the limits on mass from the AO image and from the HIRES RVs. For a given projected separation, masses above the heavy solid black line are excluded by the AO image. The heavy blue dashed line shows the lower limit for mass of the tertiary for circular orbits as a function of semimajor axis implied by the projected acceleration of $\mathcal{A} = 87 \pm 12 \text{ m s}^{-1} \text{ yr}^{-1}$ measured from the HIRES RV data. For a circular orbit with semimajor axis a and a given minimum planet mass $M_P \sin i$, the maximum projected acceleration of the star due to the planet occurs at conjunction (or opposition), and is $\mathcal{A} = GM_P \sin i a^{-2}$ (Torres 1999). Thus a strict lower limit on the tertiary mass capable of producing the measured acceleration can be defined for a given a , assuming circular orbits³². Note that this mass increases as the square of projected separation. The light blue dashed lines show the 1σ uncertainty on the minimum $M_P \sin i$ due to the uncertainty in the measured acceleration. Masses for the purported tertiary that fall below the blue dashed lines are excluded, as they do not provide sufficient acceleration at conjunction for a given semimajor axis to explain the observed trend even for an edge-on orbit. However, there could be undetected companions in the region below the blue dashed lines that are not responsible for the observed RV acceleration. The RV and AO mass curves intersect for masses comparable to the primary star, and at the

³² We note that this constraint assumes that the tertiary imposes a constant acceleration during the time spanned by the RV observations. In particular, it assumes that the systemic radial velocity has varied monotonically between the two groups of HIRES RVs shown in Figure 9. Because there is a substantial gap between these two groups of points, shorter-period orbits for the tertiary in which the acceleration changes sign twice between the two groups are possible. However, we deem these to be unlikely.

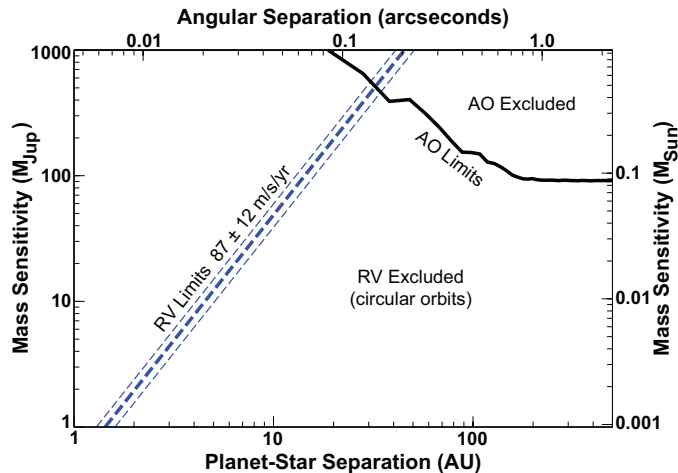


Figure 10. KELT-6 tertiary mass limits derived from the Keck AO image and measured HIRES projected acceleration versus separation in AU. The top scale shows angular separation in arcseconds corresponding to a given projected separation, assuming a distance of 222pc to the system. The AO mass limits as a function of projected separation are shown by the heavy solid black line. For a given projected separation, masses above the heavy solid black line are excluded. The heavy blue dashed line shows the lower limit on mass of the tertiary that could cause the observed projected acceleration, as a function of semimajor axis, and assuming circular orbits. The light blue dashed lines show the 1σ uncertainty in the limit due to the uncertainty in the projected acceleration. Assuming that the systematic radial velocity has varied monotonically between the two groups of HIRES RVs shown in Figure 9, masses for the tertiary causing the acceleration that fall below the dashed blue lines are excluded. However, there could be undetected companions in the region below the blue dashed lines that are not responsible for the observed RV acceleration.

diffraction-limit of a 10 m telescope on the projected separation axis. Therefore, if the speckles at the threshold of detection in Figure 5 are astrophysical, they cannot be responsible for the observed long-term acceleration in the KELT-6 radial velocities.

6. FALSE POSITIVE ANALYSIS

One of the many challenges of ground-based photometric surveys for transiting planets is the relatively high rate of astrophysical false positives prior to RV and high precision photometry follow-up observations (e.g. Latham et al. 2009). Blended eclipsing stellar binary or triple systems can mimic some of the observable signatures of transiting low-mass companions to single stars. Brown (2003) estimated the a priori detection rates of such false positives in ground-based transit surveys similar to KELT, finding a rate that was a factor of several times larger than the expected detection rate for transiting giant planets. However, for KELT-6b, we have several lines of evidence that disfavor a false positive scenario.

First, we measured the line bisector spans of the TRES spectra following Torres et al. (2007) to explore the possibility that the RV variations are actually distortions in the spectral line profiles due to a nearby unresolved eclipsing binary or stellar activity. The bisector span variations are listed in Table 1 and plotted in the bottom panel of Figure 2. The resulting bisector span variations are consistent with zero and show no correlation with the RV variations. As noted in §2.2, we did not attempt to measure line bisectors for the HIRES spectra since the PSF varies quite dramatically in the slit-fed HIRES instrument simply from guiding and spectrometer focus variations, which can cause instrumentally induced line

asymmetries that cannot be easily distinguished from stellar sources.

Second, our follow-up photometric observations of full transits in several different filters (*griz*) are all consistent with the primary transit having nearly the same depth, and are well-modeled by transits of a dark companion across a star with the limb darkening consistent with its spectroscopically measured T_{eff} and $\log g_*$ (see Figure 3 and §4.2). Since the multi-band depth difference expected for a false positive scenario depends strongly on the color difference of the blended stars, the multi-band transit observations cannot rule out all false positive configurations, but can significantly limit the allowed parameter space.

Third, we collected eight sequences of photometric observations near the time of predicted secondary eclipse (at five different epochs) in *z* and Pan-STARRS-Z bands as detailed in Table 2. The individual phased light curves and the combined binned light curve are shown in Figure 11 and cover 12 hours near the time of predicted secondary eclipse. As shown in Table 6, the fiducial predicted time of secondary eclipse has an uncertainty of ~ 16 hours. We do not find conclusive evidence of a $\gtrsim 1$ mmag secondary eclipse ingress or egress in our data. However, we do not have complete phase coverage of all the secondary eclipse times that are allowed by our global fits, and therefore we cannot place a robust lower limit on the depth of any putative secondary transit arising from a blended eclipsing binary.

Although the multi-band transit and secondary eclipse observations cannot exclude all blend scenarios, they disfavor blend scenarios in which the observed transits are due to diluted eclipses of a much fainter and redder eclipsing binary (e.g., O’Donovan et al. 2006).

Fourth, the fiducial transit derived stellar surface gravity $\log g_{*\text{transit}} = 4.074^{+0.045}_{-0.070}$ (the fiducial fit does not use a spectroscopic prior on $\log g_*$) and the HIRES spectroscopically derived surface gravity $\log g_{*\text{HIRES}} = 3.961 \pm 0.060$ are consistent within $\sim 1.5\sigma$.

Finally, our adaptive optics imaging excludes companions beyond a distance of 0.5 arcseconds from KELT-6 down to a magnitude difference of 6.0 magnitudes at 10σ confidence. See Figure 6.

We conclude that all of the available data are best explained by a Jupiter-sized, Saturn-mass companion transiting a slowly-rotating late-F star, with little or no evidence for significant contamination from blended sources.

7. EVOLUTIONARY ANALYSIS

7.1. Stellar Models and Age

We use global fit values for T_{eff} , $\log g_*$, stellar mass, and metallicity (§4 and Table 5 columns “Fit 1” and “Fit 5”), in combination with the theoretical evolutionary tracks of the Yonsei-Yale stellar models (Demarque et al. 2004), to estimate the age of the KELT-6 system. We have not directly applied a prior on the age, but rather have assumed uniform priors on $[\text{Fe}/\text{H}]$, $\log g_*$, and T_{eff} , which translates into non-uniform priors on the age. The standard version of EXOFAST uses the Torres et al. (2010) relations to estimate stellar mass and radius at each step of the MCMC chains. The top panel of Figure 12 shows the theoretical HR diagram ($\log g_*$ vs. T_{eff}) corresponding to Table 5 column “Fit 5”. We also show evolutionary tracks for masses corresponding to the $\pm 1\sigma$ extrema in the estimated uncertainty. The Torres constrained global fit values for T_{eff} and $\log g_*$ are inconsistent by more than 1σ

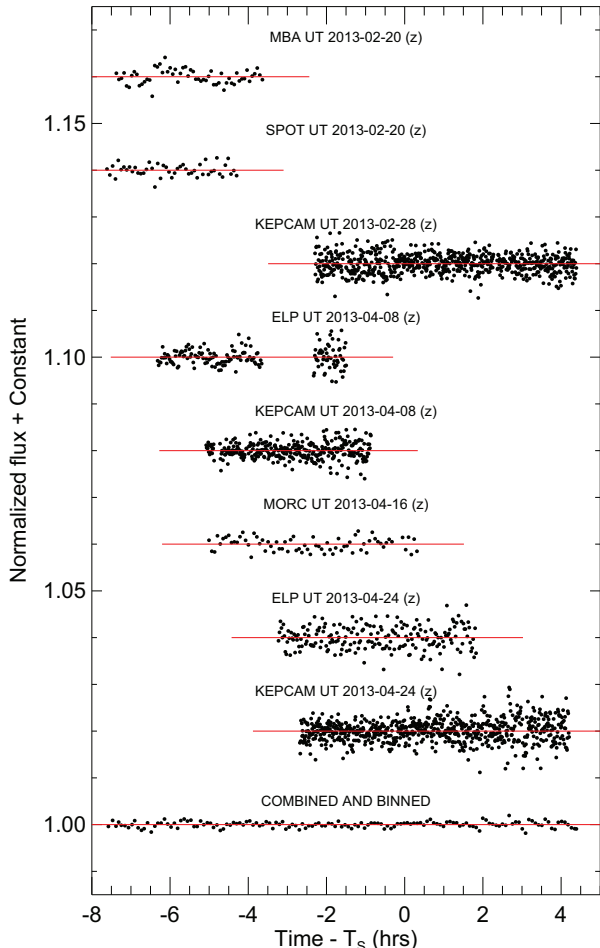


Figure 11. Phased observations of KELT-6 near the time of predicted secondary transit. The ephemeris used to phase the data is $T_0 = 2456265.51$ (BJD_{TDB}) and $P = 7.8457$ (days). The fiducial ephemeris is uncertain by ~ 0.7 days. Our observations cover only $\sim 50\%$ of the region of uncertainty. The red overlotted lines are the constant brightness models. The observatory/telescope abbreviations are the same as in Table 2. The bottom light curve shows all observations combined and binned in 5 minute intervals, and has residuals of 0.06% RMS. We find no evidence for a secondary transit in the data.

with the Yonsei-Yale track corresponding to the stellar mass and metallicity preferred by this global fit. To investigate the inconsistency, we modified EXOFAST to use the Yonsei-Yale models rather than the Torres et al. (2010) relations to estimate stellar mass and radius at each MCMC step. The bottom panel of Figure 12 is the same as the top panel, but for the fiducial Yonsei-Yale constrained global fit corresponding to Table 5 column “Fit 1”. The intersection of global fit values for T_{eff} and $\log g_*$ now fall near the Yonsei-Yale track at 6.1 ± 0.2 Gyr, where the uncertainty does not include possible systematic errors in the adopted evolutionary tracks. The Torres constrained global fit yields an age that is about 25% younger, and planet mass and radius that is larger by $\sim 4-7\%$. Although we cannot explain the inconsistency between the Torres constrained global fit and the Yonsei-Yale track, we expect that it may be due to slight inaccuracies in the Yonsei-Yale models and/or the Torres et al. (2010) relations for metal poor stars. We adopt the Yonsei-Yale constrained global fit for the analyses in this paper.

KELT-6 is evidently a late-F star that is just entering the subgiant stage of evolution. To check that the isochrone age

is consistent with other parameters of KELT-6, we use the gyrochronology relations of Barnes (2007) to compute the age based on the rotation period of the star and its $B-V$ color. We checked the KELT light curve for periodic variability associated with spot modulation as an indicator of P_{rot} , but we were unable to detect any significant sinusoidal variability beyond the photometric noise. Lacking a direct measurement, we estimated P_{rot} using the projected rotational velocity from §3.2 and the stellar radius from the adopted global fit in §4 to be $P_{\text{rot}}/\sin i_{\text{rot}} = 16.2 \pm 3.8$ days. Harris & Uppgren (1964) photoelectrically measured magnitudes and colors of KELT-6 and found $B-V = 0.49 \pm 0.008$. Tycho (Høg et al. 2000) measured B_T and V_T (Table 4), and through the filter transformations described in ESA (1997), the Tycho-based color is $B-V = 0.415 \pm 0.069$. Because the Harris & Uppgren (1964) precision is much higher than Tycho’s, and since the Tycho color is consistent with the Harris & Uppgren (1964) color at nearly 1σ , we adopt the Harris & Uppgren (1964) color for this analysis. In particular, we are worried about inaccuracies in the Tycho-to-Johnson filter-band transformations, especially for metal-poor stars; Høg et al. (2000) state that these filter-band transformations are approximate. Based on the adopted rotation period and $B-V$ color of the star, we calculate the maximum predicted age (subject to the inclination of the rotation axis to our line of sight) to be 5.7 ± 1.3 Gyr, which is fully consistent with the isochrone age. We note that if the Tycho fiducial color is used with the adopted rotation period, the Barnes (2007) relations yield an unrealistically large age of 46 Gyr, due to the fact that these relations break down for stars with $B-V \lesssim 0.4$, which generally have small or non-existent convective envelopes.

7.2. Insolation Evolution

In an investigation of transiting giant exoplanets, Demory & Seager (2011) found that for planets insolated beyond the threshold of $2 \times 10^8 \text{ erg s}^{-1} \text{ cm}^{-2}$ the radii are inflated compared to those planets with lower levels of insolation. KELT-6b currently has incident flux well above that threshold, and is a mildly inflated hot Saturn with a density of $0.248^{+0.059}_{-0.050} \text{ g cm}^{-3}$. It follows the insolation-inflation trend displayed in Figure 1 of Demory & Seager (2011). However, it is worth investigating whether KELT-6b has always been insolated above the Demory & Seager (2011) threshold. If it turns out that KELT-6b only recently began receiving enhanced irradiation, this could provide an empirical probe of the timescale of inflation mechanisms (see Assef et al. 2009 and Spiegel & Madhusudhan 2012).

To answer that question, we simulate the reverse and forward evolution of the star-planet system, using the fiducial global fit parameters listed in Table 6 as the present boundary conditions. This analysis is not intended to examine circularization of the planet’s orbit, tidal locking to the star, or any type of planet-planet or planet-disk interaction or migration. Rather, it is a way to infer the insolation of the planet over time due to the changing luminosity of the star and changing star-planet separation.

We include the evolution of the star, which is assumed to follow the YREC stellar model corresponding to $M = 1.1 M_{\odot}$ and $Z = 0.0162$ (Siess et al. 2000). We also assume that the stellar rotation was influenced only by tidal torques due to the planet, with no magnetic wind and treating the star like a solid body. Although the fiducial model from §4.2 has an eccentric orbit, we assume a circular orbit throughout the full insolation

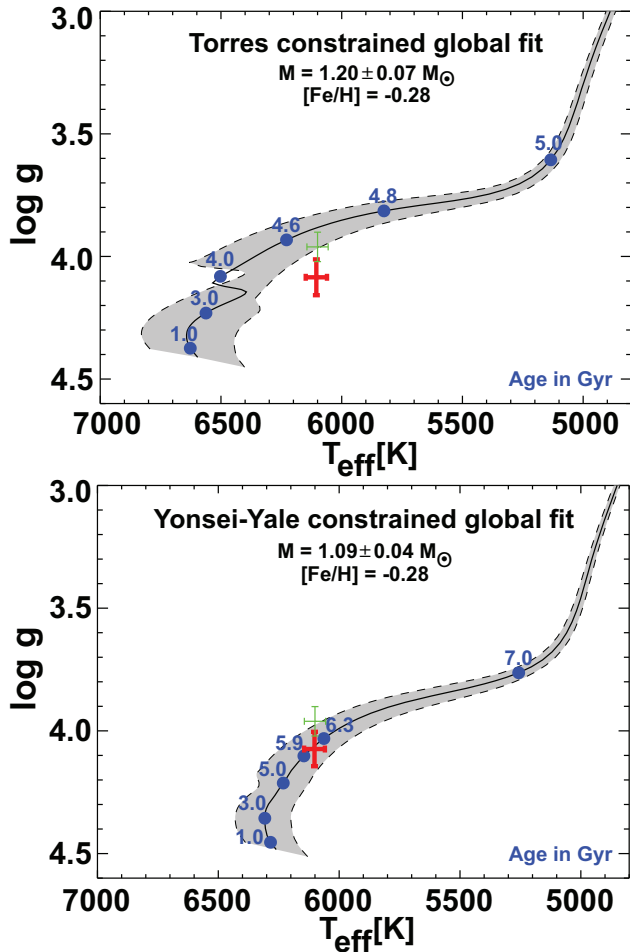


Figure 12. Theoretical HR diagrams based on Yonsei-Yale stellar evolution models (Demarque et al. 2004). The gray swaths represent the evolutionary track for the best-fit values of the mass and metallicity of the host star from the global fits corresponding to Table 5 columns “Fit 1” (bottom panel) and “Fit 5” (top panel) and discussed in §4. The tracks for the extreme range of 1σ uncertainties on M_* and $[\text{Fe}/\text{H}]$ are shown as dashed lines bracketing each gray swath. *Top panel:* The Yonsei-Yale track based on the Torres constrained global fit corresponding to Table 5 column “Fit 5” (see §7 for explanation). *Bottom panel:* The Yonsei-Yale track based on a Yonsei-Yale constrained fiducial global fit corresponding to Table 5 column “Fit 1”. The thick red crosses show T_{eff} and $\log g_*$ from the EXOFAST global fit analyses. The thin green crosses show the inferred T_{eff} and $\log g_*$ from the HIRES spectroscopic analysis alone. The blue dots represent the location of the star for various ages in Gyr. The Torres constrained global fit is inconsistent with the Yonsei-Yale track at $> 1\sigma$. We adopt the Yonsei-Yale constrained global fit represented in the bottom panel resulting in a slightly evolved star with an estimated age of 6.1 ± 0.2 Gyr, where the uncertainty does not include possible systematic errors in the adopted evolutionary tracks.

analysis. The results of our simulations are shown in Figure 13. We tested a range of values for the tidal quality factor of the star Q_* , from $\log Q_* = 5$ to $\log Q_* = 9$. We find that this system is highly insensitive to the value of Q_* , because tides are not important for this system for the parameter ranges we analyzed. In all cases, KELT-6b has always received more than enough flux from its host to keep the planet irradiated beyond the Demory & Seager (2011) insolation threshold required for inflation.

8. DISCUSSION

From our global fit to the spectroscopy, light curves, and HIRES RVs, we find that KELT-6b is a metal-poor hot Sat-

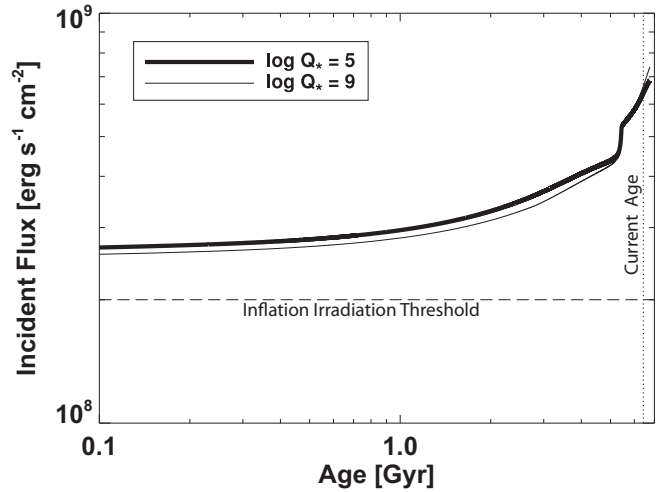


Figure 13. Change in incident flux for KELT-6b, with test values of $\log Q_* = 5$ and $\log Q_* = 9$ for KELT-6. This system is clearly insensitive to the value of Q_* in the range we analyzed. In both cases, the planet has always received more than enough flux from its host to keep the planet irradiated beyond the insolation threshold of $2 \times 10^8 \text{ erg s}^{-1} \text{ cm}^{-2}$ identified by Demory & Seager (2011).

urn with a measured mass $M_p = 0.430^{+0.045}_{-0.046} M_{\text{Jup}}$ and radius $R_p = 1.193^{+0.130}_{-0.077} R_{\text{Jup}}$. It is on an orbit with eccentricity $e = 0.22^{+0.12}_{-0.10}$ and semimajor axis of $a = 0.07939^{+0.00100}_{-0.00099}$ AU. The host KELT-6 is a slightly evolved late-F star with a mass $M_* = 1.085 \pm 0.043 M_\odot$, radius $R_* = 1.580^{+0.16}_{-0.094} R_\odot$, effective temperature $T_{\text{eff}} = 6102 \pm 43$ K, and a likely age of 6.1 ± 0.2 Gyr. Because of its larger semimajor axis (compared to a typical hot Jupiter), KELT-6b receives a moderate stellar insolation flux of $\langle F \rangle = 6.53^{+0.92}_{-0.76} \times 10^8 \text{ erg s}^{-1} \text{ cm}^{-2}$, implying a moderate equilibrium temperature of $T_{\text{eq}} = 1313^{+59}_{-38}$ K assuming zero albedo and perfect redistribution. The surface gravity and density of KELT-6b are $\log g_p = 2.868^{+0.063}_{-0.081}$ and $\rho_p = 0.311^{+0.069}_{-0.076} \text{ g cm}^{-3}$. We do not have in-transit KELT-6b RV data, so we have no Rossiter-McLaughlin effect constraint on the projected rotation axis of its host star.

Even among the ever growing list of known transiting exoplanets, KELT-6b is unique. In Figure 14 we compare planet mass as a function of the orbital period (top panel), incident flux as a function of $\log g_p$ (middle panel), and $[\text{Fe}/\text{H}]$ as a function of $\log g_p$ (bottom panel), for the group of all transiting hot gas giants orbiting bright hosts, which we define as $m > 0.1 M_{\text{Jup}}$, $P < 20$ days, and host star $V < 11.0$. Within that group, KELT-6 is among the 20 brightest host stars, and KELT-6b has the third longest orbital period (top panel), second lowest mass (top panel), and is the most metal-poor (bottom panel). In the larger group of all transiting exoplanets discovered by ground-based transit surveys, KELT-6b has the sixth longest period and the second longest transit duration. To our knowledge, the high precision photometric follow-up observations reported in this work include the longest duration transit ever fully observed from a single ground-based telescope.

Perhaps the most significant importance of the KELT-6b discovery is that it has similar $\log g_p$ and incident flux as HD 209458b (middle panel), one of the most studied and best understood exoplanets, but its host has a metallicity that is lower than HD 209458 by $\sim 0.3 \text{ dex}^{33}$. This, combined

³³ While HAT-P-1b, WASP-13b, WASP-35b, and WASP-62b have $\log g_p$

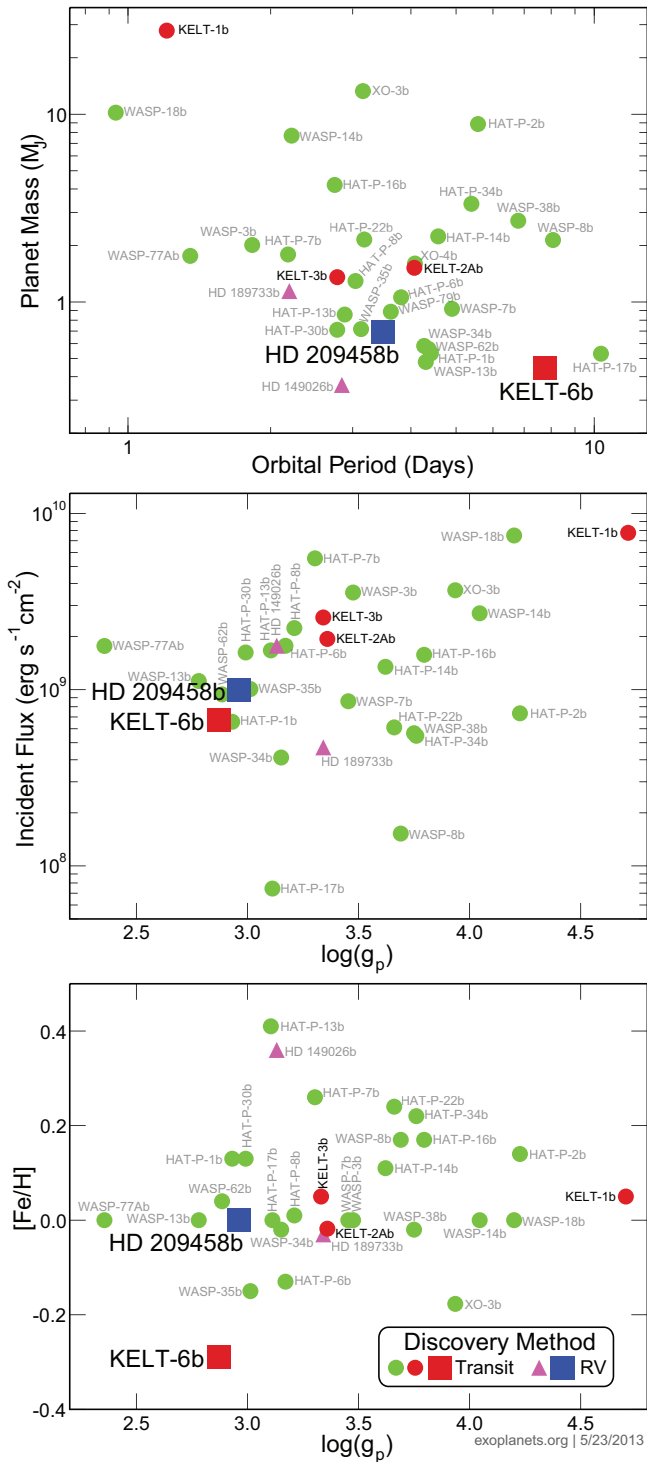


Figure 14. Comparisons of bright, transiting, hot gas giants with $m > 0.1 M_{\text{Jup}}$, $P < 20$ days, and host star $V < 11.0$. The three RV discovered planets are shown as magenta filled triangles (HD 189733b and HD 149026b) and a large blue filled square (HD 209458b). All other transits were discovered by ground-based transit surveys. No Kepler targets currently meet the specified criteria for inclusion in the group. The KELT-north survey planets are shown as red filled circles, except KELT-6b which is shown as a large red filled square. All other planets are shown as green filled circles. *Top panel:* Planet mass as a function of the orbital period. Both KELT-6b and HD 189733b are sub-Jupiter mass planets. *Middle panel:* Incident flux as a function of planet surface gravity. KELT-6b has surface gravity and incident flux similar to HD 209458b. All else being equal, objects in the top left have the highest transmission spectroscopy signal. *Bottom panel:* $[\text{Fe}/\text{H}]$ as a function of planet surface gravity. KELT-6b has metallicity lower than HD 209458b by ~ 0.3 dex. KELT-6b and HD 209458b offer an opportunity to perform a comparative measurement of two similar planets in similar environments around stars of very different metallicities.

with the fact that KELT-6 is relatively bright at $V \sim 10.4$ (see Figure 15), means that this system provides an opportunity to perform comparative measurements of two similar planets in similar environments around stars of very different metallicities. In particular, we advocate attempting to acquire both transmission and secondary eclipse spectroscopy from the ground and space. The resulting spectra can be compared directly with those already in hand for HD 209458b (e.g., Knutson et al. 2008; Désert et al. 2008; Sing et al. 2008; Snellen et al. 2008; Swain et al. 2009). Such direct comparisons may, for example, elucidate the effect of bulk composition of the planet atmosphere on the cause of atmospheric temperature inversions. We note that, in order to properly plan for secondary eclipse observations, additional radial velocity observations will be needed to more precisely constrain the eccentricity of KELT-6b and so predict the time of secondary eclipse. Such observations will also be important for characterizing the orbit of the tertiary object in the KELT-6 system. For these reasons, KELT-6b should prove to be a very interesting object for further study.

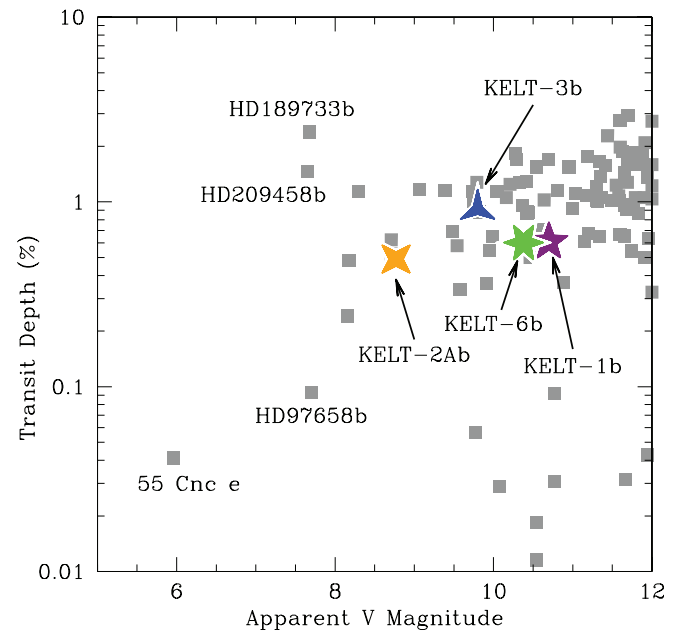


Figure 15. Transit depth assuming no limb darkening as a function of the host star apparent V magnitude for transiting systems with relatively bright ($V \leq 12$) hosts. KELT-6b is shown as the green six-pointed star. The other KELT discoveries are also shown, and the transiting systems with very bright hosts ($V \leq 8$) are labeled. Systems in the top left tend to be the most amenable to detailed spectroscopic and photometric studies.

K.A.C. was supported by a NASA Kentucky Space Grant Consortium Graduate Fellowship. Early work on KELT-North was supported by NASA Grant NNG04GO70G. J.A.P. and K.G.S. acknowledge support from the Vanderbilt Office of the Provost through the Vanderbilt Initiative in Data-intensive Astrophysics. E.L.N.J. gratefully acknowledges the support of the National Science Foundation's PREST program, which helped to establish the Peter van de Kamp Observatory through grant AST-0721386. K.G.S. acknowledges the

and incident flux similar to HD 209458b, none of them are metal poor except for WASP-35b, which has a metallicity of $[\text{Fe}/\text{H}] = -0.15$.

support of the National Science Foundation through PAARE Grant AST-0849736 and AAG Grant AST-1009810. Work by B.S.G. and T.G.B. was partially supported by NSF CAREER Grant AST-1056524. K.P. acknowledges support from NASA grant NNX09AB29G and NSF award number 1108686. We thank the anonymous referee for a thoughtful reading of the manuscript and for useful suggestions. We thank Geoff Marcy and Howard Isaacson for Keck HIRES observations, calibration, and reduction of spectra to 1-D form. The authors wish to recognize and acknowledge the very significant cultural role and reverence that the summit of Mauna Kea has always had within the indigenous Hawaiian community. We are most fortunate to have the opportunity to conduct observations from this mountain. The TRES and KeplerCam observations were obtained with partial support from the Kepler Mission through NASA Cooperative Agreement NNX11AB99A with the Smithsonian Astrophysical Observatory (PI: D.W.L.). A portion of this work was supported by the National Science Foundation under grant Nos. AST-1203023. We thank Roberto Zambelli of Societa Astronomica Lunae for participation in the KELT followup network. This work has made use of NASA's Astrophysics Data System, the Exoplanet Orbit Database at exoplanets.org, the Extrasolar Planet Encyclopedia at exoplanet.eu (Schneider et al. 2011), the SIMBAD database operated at CDS, Strasbourg, France, and Systemic (Meschiari et al. 2009).

REFERENCES

- Alard, C. 2000, *A&AS*, 144, 363
 Alard, C., & Lupton, R. H. 1998, *ApJ*, 503, 325
 Alonso, R., Brown, T. M., Torres, G., et al. 2004, *ApJ*, 613, L153
 Alsubai, K. A., Parley, N. R., Bramich, D. M., et al. 2011, *MNRAS*, 417, 709
 Anderson, D. R., Collier Cameron, A., Delrez, L., et al. 2013, arXiv:1310.5654
 Assef, R. J., Gaudi, B. S., & Stanek, K. Z. 2009, *ApJ*, 701, 1616
 Baglin, A. 2003, *Advances in Space Research*, 31, 345
 Bakos, G. Á., Noyes, R. W., Kovács, G., et al. 2007, *ApJ*, 656, 552
 Baraffe, I., Chabrier, G., Allard, F., & Hauschildt, P. H. 2008, *A&A*, 337, 403
 Barnes, S. A. 2007, *ApJ*, 669, 1167
 Beatty, T. G., Pepper, J., Siverd, R. J., et al. 2012, *ApJ*, 756, L39
 Borucki, W. J., Koch, D., Basri, G., et al. 2010, *Science*, 327, 977
 Brown, T. M. 2003, *ApJ*, 593, L125
 Brown, T. M., Baliber, N., Bianco, F., et al. 2013, *PASP*, 125, 1031
 Buchhave, L. A., Bakos, G. Á., Hartman, J. D., et al. 2010, *ApJ*, 720, 1118
 Buchhave, L. A., Latham, D. W., Johansen, A., et al. 2012, *Nature*, 486, 375
 Burrows, A., Hubeny, I., Budaj, J., & Hubbard, W. B. 2007, *ApJ*, 661, 502
 Butler, R. P., Marcy, G. W., Williams, E., McCarthy, C., Dosanji, P., Vogt, S. S. 1996, *PASP*, 108, 500
 Charbonneau, D., Brown, T. M., Latham, D. W., & Mayor, M. 2000, *ApJ*, 529, L45
 Chubak, C., Marcy, G. W., Fischer, D. A., et al. 2012, arXiv:1207.6212
 Claret, A., & Bloemen, S. 2011, *A&A*, 529, A75
 Collier Cameron, A., Bouchy, F., Hébrard, G., et al. 2007, *MNRAS*, 375, 951
 Collier Cameron, A., Wilson, D. M., West, R. G., et al. 2007, *MNRAS*, 380, 1230
 Crepp, J. R., Johnson, J. A., Howard, A. W., et al. 2012, *ApJ*, 761, 39
 Cutri, R. M., Skrutskie, M. F., van Dyk, S., et al. 2003, *yCat*, 2246, 0
 Cutri, R. M., Wright, E. L., Bauer, J., et al. 2012, *yCat*, 2311, 0
 Dawson, R. I., & Murray-Clay, R. A. 2013, *ApJ*, 767, 24
 Demarque, P., Woo, J.-H., Kim, Y.-C., & Yi, S. K. 2004, *ApJS*, 155, 667
 Demory, B.-O., & Seager, S. 2011, *ApJS*, 197, 12
 Désert, J.-M., Vidal-Madjar, A., Lecavelier Des Etangs, A., et al. 2008, *A&A*, 492, 585
 Eastman, J., Siverd, R., & Gaudi, B. S. 2010, *PASP*, 122, 935
 Eastman, J., Gaudi, B. S., & Agol, E. 2013, *PASP*, 125, 83
 ESA. 1997, *The Hipparcos and Tycho Catalogues* (ESA SP-1200; Noordwijk: ESA)
 Ford, E.B. 2006, *ApJ*, 642, 505
 Fulton, B. J., Shporer, A., Winn, J. N., Holman, M. J., Pál, A., & Gazak, J. Z. 2011, *AJ*, 142, 84
 Fűrész, G. 2008, PhD thesis, Univ. Szeged
 Gould, A., & Morgan, C. W. 2003, *ApJ*, 585, 1056
 Harris, D. L., & Upgren, A. R. 1964, *ApJ*, 140, 151
 Hartman, J. D., Gaudi, B. S., Holman, M. J., et al. 2008, *ApJ*, 675, 1254
 Hauschildt, P. H., Allard, F., Ferguson, J., Baron, E., & Alexander, D. R. 1999, *ApJ*, 525, 871
 Henry, G. W., Marcy, G. W., Butler, R. P., Baron, E., & Vogt, S. S. 2000, *ApJ*, 529, L41
 The Hipparcos and Tycho Catalogues 1997, ESA SP-1200
 Høg, E., Fabricius, C., Makarov, V. V., et al. 2000, *A&A*, 355, L27
 Howard, A. W., Johnson, J. A., Marcy, G. W., et al. 2011, *ApJ*, 726, 73
 Jensen, E. L. N. 2013, *Tapir, Astrophysics Source Code Library*, record ascl:1306.007
 Johnson, J. A., Howard, A. W., Marcy, G. W., et al. 2010, *PASP*, 122, 149
 Knutson, H. A., Charbonneau, D., Allen, L. E., Burrows, A., & Megeath, S. T. 2008, *ApJ*, 673, 526
 Kovács, G., Zucker, S., & Mazeh, T. 2002, *A&A*, 391, 369
 Kovács, G., Bakos, G., & Noyes, R. W. 2005, *MNRAS*, 356, 557
 Latham, D. W., Bakos, G. A., Torres, G., et al. 2009, *ApJ*, 704, 1107
 Lucy, L. B., & Sweeney, M. A. 1971, *AJ*, 76, 544
 Madhusudhan, N., & Seager, S. 2010, *ApJ*, 725, 261
 Marcy, G. W., & Butler, R. P. 1992, *PASP*, 104, 270
 Martin, D. C., Fanson, J., Schiminovich, D., et al. 2005, *ApJ*, 619, L1
 McCullough, P. R., Stys, J. E., Valenti, J. A., et al. 2006, *ApJ*, 648, 1228
 Meschiari, S., Wolf, A. S., Rivera, E., et al. 2009, *PASP*, 121, 1016
 O'Donovan, F. T., Charbonneau, D., Torres, G., et al. 2006, *ApJ*, 644, 1237
 Pepper, J., Gould, A., & DePoy, D. L. 2003, *Acta Astronomica*, 53, 213
 Pepper, J., Pogge, R. W., DePoy, D. L., et al. 2007, *PASP*, 119, 923
 Pepper, J., Siverd, R. J., Beatty, T. G., et al. 2013, *ApJ*, 773, 64
 Ribas, I., & Miralda-Escudé, J. 2007, *A&A*, 464, 779
 Richmond, M. W., Droege, T. F., Gombert, G., et al. 2000, *PASP*, 112, 397
 Sato, B., Fischer, D. A., Henry, G. W., Laughlin, G., et al. 2005, *ApJ*, 633, 465
 Schneider, J., Dedieu, C., Le Sidaner, P., Savalle, R., & Zolotukhin, I. 2011, *A&A*, 532, A79
 Siess, L., Dufour, E., & Forestini, M. 2000, *A&A*, 358, 593
 Sing, D. K., Vidal-Madjar, A., Désert, J.-M., Lecavelier des Etangs, A., & Ballester, G. 2008, *ApJ*, 686, 658
 Siverd, R. J., Beatty, T. G., Pepper, J., et al. 2012, *ApJ*, 761, 123
 Skrutskie, M. F., Cutri, R. M., Stiening, R., et al. 2006, *AJ*, 131, 1163
 Snellen, I. A. G., Albrecht, S., de Mooij, E. J. W., & Le Poole, R. S. 2008, *A&A*, 487, 357
 Spiegel, D. S., & Madhusudhan, N. 2012, *ApJ*, 756, 132
 Stetson, P. B. 1987, *PASP*, 99, 191
 Swain, M. R., Tinetti, G., Vasisht, G., et al. 2009, *ApJ*, 704, 1616
 Torres, G. 1999, *PASP*, 111, 169
 Torres, G., Bakos, G. Á., Kovács, G., et al. 2007, *ApJ*, 666, 121
 Torres, G., Winn, J. N., & Holman, M. J. 2008, *ApJ*, 677, 1324
 Torres, G., Andersen, J., & Giménez, A. 2010, *A&A Rev.*, 18, 67
 Valenti, J. A., & Piskunov, N. 1996, *A&AS*, 118, 595
 Valenti, J. A., & Fischer, D. A. 2005, *ApJS*, 159, 141
 Vogt, S. S., Allen, S. L., Bigelow, B. C., et al. 1994, *Proc. SPIE*, 2198, 362
 Winn, J. N. 2009, in *IAU Symp. 253, Transiting Planets*, ed. F. Pont, D. D. Sasselov, & M. J. Holman (Cambridge: Cambridge Univ. Press), 99
 Winn, J. N. 2010, in *Exoplanets*, ed. S. Seager, Tucson:University of Arizona Press, 55
 Wright, E. L., Eisenhardt, P. R. M., Mainzer, A. K., et al. 2010, *AJ*, 140, 1868
 Wright, E. L., Fakhouri, O., Marcy, G. W., et al. 2011, *PASP*, 123, 412
 Wright, J. T. 2012, *PASP*, 117, 657
 Zacharias, N., Monet, D. G., Levine, S. E., et al. 2004, *Bulletin of the American Astronomical Society*, 36, 1418

Table 4
KELT-6 Stellar Properties

Parameter	Description (Units)	Value	Source	Ref.
Names		TYC 2532-556-1 BD+31 2447 Weis 32018		
α_{J2000}		13:03:55.647	Tycho-2	1
δ_{J2000}		+30:38:24.26	Tycho-2	1
FUV_{GALEX}		20.328 ± 0.242	GALEX	2
NUV_{GALEX}		14.263 ± 0.190	GALEX	2
B_T		10.837 ± 0.049	Tycho-2	1
V_T		10.418 ± 0.047	Tycho-2	1
$B_T - V_T$		0.49 ± 0.008	Harris	3
V		10.337 ± 0.054	TASS	4
I_C		9.745 ± 0.061	TASS	4
J		9.302 ± 0.05	2MASS	5
H		9.137 ± 0.05	2MASS	5
K_S		9.083 ± 0.05	2MASS	5
WISE1		11.706 ± 0.1	WISE	6
WISE2		12.38 ± 0.1	WISE	6
WISE3		14.311 ± 0.1	WISE	6
μ_α	Proper Motion in RA (mas yr ⁻¹)	-6.4 ± 0.7	NOMAD	7
μ_δ	Proper Motion in Dec. (mas yr ⁻¹)	15.6 ± 0.7	NOMAD	7
γ_{abs}	Absolute Systemic RV (km s ⁻¹)	1.1 ± 0.2	This Paper ^a	
.....	Spectral Type	F8±1	This Paper	
d	Distance (pc)	222 ± 8	This Paper	
.....	Age (Gyr)	6.1 ± 0.2	This Paper ^b	
A_V	Visual Extinction	0.01 ± 0.02	This Paper	
(U^c, V, W)	Galactic Space Velocities (km s ⁻¹)	($-6.3 \pm 0.9, 23.2 \pm 0.8, 6.9 \pm 0.2$)	This Paper ^d	

Note. — Magnitudes are on the AB system. Uncertainties for the 2MASS and WISE bands were increased to 0.05 mag and 0.10 mag, respectively, to account for systematic uncertainties. 1=Høg et al. (2000), 2=Martin et al. (2005), 3=Harris & Upgren (1964), 4=Richmond et al. (2000), 5=Skrutskie et al. (2006); Cutri et al. (2003), 6=Wright et al. (2010); Cutri et al. (2012). 7=Zacharias et al. (2004).

^a The absolute RV uncertainty is due to the systematic uncertainties in the absolute velocities of the RV standard stars.

^b The uncertainty does not include possible systematic errors in the adopted evolutionary tracks.

^c We adopt a right-handed coordinate system such that positive U is toward the Galactic Center.

^d See §3.3

Table 5

Median Values and 68% Confidence Intervals for Selected Physical and Orbital Parameters of the KELT-6 System from 6 Global Fits Described in §4.2

Parameter	Units	Fit 1 (adopted)	Fit 2	Fit 3	Fit 4	Fit 5	Fit 6
Global Fit Parameters:							
Number of Transits...	5 or 16	5	5	5	5	5	16
M_* and R_* Constraint	Torres or Yonsei-Yale	Yonsei-Yale	Yonsei-Yale	Yonsei-Yale	Yonsei-Yale	Torres	Yonsei-Yale
Orbital Constraint	Circular or Eccentric	Eccentric	Circular	Circular	Eccentric	Eccentric	Eccentric
$\log g_*$ Prior	Prior or No Prior	No Prior	Prior	No Prior	Prior	No Prior	No Prior
Stellar Parameters:							
T_{eff}	Effective temp (K)	6102 ± 43	6101 ± 43	6103 ± 43	6102 ± 44	6105 ± 44	6109 ± 44
[Fe/H]	Metallicity	$-0.281^{+0.039}_{-0.038}$	$-0.285^{+0.040}_{-0.038}$	$-0.282^{+0.039}_{-0.037}$	$-0.284^{+0.040}_{-0.039}$	$-0.280^{+0.039}_{-0.039}$	$-0.284^{+0.039}_{-0.038}$
$\log g_*$	Surface gravity (cgs)	$4.074^{+0.045}_{-0.070}$	$4.057^{+0.036}_{-0.037}$	$4.083^{+0.022}_{-0.042}$	$4.012^{+0.049}_{-0.054}$	$4.085^{+0.046}_{-0.073}$	$4.064^{+0.049}_{-0.068}$
M_*	Mass (M_\odot)	$1.085^{+0.043}_{-0.040}$	$1.086^{+0.033}_{-0.036}$	$1.081^{+0.032}_{-0.034}$	$1.110^{+0.041}_{-0.041}$	$1.199^{+0.065}_{-0.060}$	$1.090^{+0.042}_{-0.040}$
R_*	Radius (R_\odot)	$1.580^{+0.160}_{-0.094}$	$1.615^{+0.086}_{-0.078}$	$1.562^{+0.091}_{-0.046}$	$1.720^{+0.140}_{-0.110}$	$1.640^{+0.170}_{-0.100}$	$1.600^{+0.160}_{-0.100}$
Planetary Parameters:							
M_P	Mass (M_J)	$0.430^{+0.045}_{-0.046}$	$0.438^{+0.038}_{-0.037}$	$0.436^{+0.037}_{-0.037}$	$0.446^{+0.044}_{-0.043}$	$0.461^{+0.049}_{-0.048}$	$0.431^{+0.046}_{-0.046}$
R_P	Radius (R_J)	$1.193^{+0.130}_{-0.077}$	$1.228^{+0.080}_{-0.070}$	$1.178^{+0.083}_{-0.043}$	$1.304^{+0.110}_{-0.093}$	$1.240^{+0.140}_{-0.085}$	$1.206^{+0.120}_{-0.085}$
$\log g_P$	Surface gravity	$2.868^{+0.063}_{-0.081}$	$2.855^{+0.057}_{-0.061}$	$2.885^{+0.049}_{-0.061}$	$2.810^{+0.065}_{-0.068}$	$2.865^{+0.064}_{-0.083}$	$2.862^{+0.064}_{-0.080}$
e	Eccentricity	$0.22^{+0.12}_{-0.10}$	—	—	$0.27^{+0.11}_{-0.12}$	$0.22^{+0.12}_{-0.10}$	$0.22^{+0.12}_{-0.10}$
a	Semi-major axis (AU)	$0.079^{+0.00100}_{-0.00099}$	$0.079^{+0.00080}_{-0.00087}$	$0.079^{+0.00078}_{-0.00085}$	$0.080^{+0.00098}_{-0.00099}$	$0.082^{+0.00150}_{-0.00140}$	$0.080^{+0.001}_{-0.001}$
T_{eq}	Equilibrium temp (K)	1313^{+59}_{-38}	1327^{+33}_{-30}	1307^{+34}_{-20}	1364^{+48}_{-43}	1317^{+61}_{-38}	1323^{+58}_{-41}

Table 6
Adopted Median Values and 68% Confidence Intervals for the Physical and Orbital Parameters of the KELT-6 System from the Fiducial Global Fit Described in §4.2

Parameter	Units	Value (adopted)
Stellar Parameters:		
M_*	Mass (M_\odot)	$1.085^{+0.043}_{-0.040}$
R_*	Radius (R_\odot)	$1.580^{+0.16}_{-0.094}$
L_*	Luminosity (L_\odot)	$3.11^{+0.68}_{-0.39}$
ρ_*	Density (cgs)	$0.387^{+0.268}_{-0.088}$
$\log g_*$	Surface gravity (cgs)	$4.074^{+0.045}_{-0.070}$
T_{eff}	Effective temperature (K)	6102 ± 43
[Fe/H]	Metallicity	$-0.281^{+0.039}_{-0.038}$
Planetary Parameters:		
e	Eccentricity	$0.22^{+0.12}_{-0.10}$
ω_*	Argument of periastron (degrees)	80^{+10}_{-120}
P	Period (days)	7.8457 ± 0.0002
a	Semi-major axis (AU)	$0.07939^{+0.0010}_{-0.00099}$
M_P	Mass (M_J)	$0.430^{+0.045}_{-0.046}$
R_P	Radius (R_J)	$1.193^{+0.13}_{-0.077}$
ρ_P	Density (cgs)	$0.311^{+0.069}_{-0.076}$
$\log g_P$	Surface gravity	$2.868^{+0.063}_{-0.081}$
T_{eq}	Equilibrium temperature (K)	1313^{+59}_{-38}
Θ	Safronov number	$0.0521^{+0.0059}_{-0.0061}$
$\langle F \rangle$	Incident flux ($10^9 \text{ erg s}^{-1} \text{ cm}^{-2}$)	$0.653^{+0.092}_{-0.076}$
RV Parameters:		
T_C	Time of inferior conjunction (BJD_{TDB})	$2456269.3399^{+0.0071}_{-0.0072}$
T_P	Time of periastron (BJD_{TDB})	$2456269.2^{+1.7}_{-2.5}$
K	RV semi-amplitude (m s^{-1})	$42.8^{+4.5}_{-4.2}$
$M_P \sin i$	Minimum mass (M_J)	$0.430^{+0.045}_{-0.046}$
M_P/M_*	Mass ratio	$0.000378^{+0.000036}_{-0.000037}$
u	RM linear limb darkening	$0.6035^{+0.0040}_{-0.0039}$
γ_{HIRES}	m s^{-1}	-3.1 ± 3.2
$\dot{\gamma}_{\text{HIRES}}$	RV slope ($\text{m s}^{-1} \text{ day}^{-1}$)	-0.239 ± 0.037
$e \cos \omega_*$	$0.02^{+0.13}_{-0.14}$
$e \sin \omega_*$	$0.05^{+0.23}_{-0.22}$
$f(m_1, m_2)$	Mass function (M_J)	$0.000000061^{+0.000000020}_{-0.000000017}$
Primary Transit Parameters:		
R_P/R_*	Radius of the planet in stellar radii	$0.07761^{+0.0010}_{-0.00092}$
a/R_*	Semi-major axis in stellar radii	$10.79^{+0.60}_{-0.89}$
i	Inclination (degrees)	$88.81^{+0.79}_{-0.91}$
b	Impact parameter	$0.20^{+0.14}_{-0.13}$
δ	Transit depth	$0.00602^{+0.00016}_{-0.00014}$
T_0	Best-fit linear ephemeris from transits (BJD_{TDB})	$2456347.796793 \pm 0.000364$
P_{Transit}	Best-fit linear ephemeris period from transits (days)	7.8456314 ± 0.0000459
T_{FWHM}	FWHM duration (days)	$0.212^{+0.039}_{-0.029}$
τ	Ingress/egress duration (days)	$0.0175^{+0.0039}_{-0.0028}$
T_{14}	Total duration (days)	$0.230^{+0.043}_{-0.032}$
P_T	A priori non-grazing transit probability	$0.091^{+0.038}_{-0.021}$
$P_{T,G}$	A priori transit probability	$0.107^{+0.044}_{-0.024}$
Secondary Eclipse Parameters:		
T_S	Time of eclipse (BJD_{TDB})	$2456265.51^{+0.66}_{-0.70}$
b_S	Impact parameter	$0.22^{+0.18}_{-0.14}$
$T_{S,\text{FWHM}}$	FWHM duration (days)	$0.231^{+0.073}_{-0.051}$
τ_S	Ingress/egress duration (days)	$0.0194^{+0.0083}_{-0.0048}$
$T_{S,14}$	Total duration (days)	$0.251^{+0.081}_{-0.058}$
P_S	A priori non-grazing eclipse probability	$0.084^{+0.010}_{-0.010}$
$P_{S,G}$	A priori eclipse probability	$0.098^{+0.020}_{-0.012}$